Optimization and Verification of a new Analytical Radiative Transfer Model

Philipp Michael Maximilian Grötsch

DIPLOMA THESIS

München 2011

Optimization and Verification of a new Analytical Radiative Transfer Model

Philipp Michael Maximilian Grötsch

Diplomarbeit
am Deutschen Luft- und Raumfahrtzentrum (DLR)
Oberpfaffenhofen
Institut für Experimentelle Verfahren
bei
Dr. Peter Gege

vorgelegt von
Philipp Michael Maximilian
Grötsch
aus München

München, den 25. Juli 2011

Erstgutachter: Prof. Dr. M. Dameris
Zweitgutachter: Prof. Dr. B. Mayer

Abstract

The analysis of satellite or airborne remote sensing data relies on reference measurements on the ground. For water covered areas, spectral reference measurements need to be carried out in and above the water column. Due to the wave-focusing effect a high variability is induced to the measurements. A new analytical model allows to account for this effect by treating the direct and diffuse parts of the light field separately. Parameterizations of the downwelling direct and diffuse attenuation coefficients, K_{dd} and K_{ds}, were developed in this study. For this purpose numerical simulations with the well established radiative transfer model Hydrolight 5.0 were carried out. The program was modified to calculate the direct and diffuse components separately. The developed analytical parameterization was verified against these calculations and compared to a recently published semi-analytical model by Pan and Zimmerman, which also treats direct and diffuse radiation separately. The diffuse part of this model could be improved with the developed parameterization concerning the sun zenith angle dependency. The physically meaningful, new analytical model performs better, on a wide range of simulated water compositions than the original, and even the improved Pan-Zimmerman model. The new parameterization is not restricted to absorption dominated water bodies. Field measurements were performed to collect a dataset which is suitable to independently validate the model. The model was fitted to these field measurements and the results of one fit parameter, the sensor depth, were compared to independent measurements. The model yields equally small mean errors and standard deviations for clear and overcast sky conditions, even at extremely high sun zenith angles. In comparison to a widely used model of Gordon, the mean standard deviation is decreased by a factor of five, which is a result of the successful correction of the wave focusing effect. The absolute differences are on average by a factor of three lower due to the improved parameterizations of K_{dd} and K_{ds}.

Zusammenfassung

Die Interpretation von Satelliten- oder Flugzeugfernerkundungsdaten ist abhängig von Referenzmessungen am Boden. Für Wasserflächen müssen spektrale Referenzmessungen sowohl in als auch über der Wassersäule erfolgen. Aufgrund des 'wave-focusing' Effekts sind Unterwassermessungen mit einer starken Variabilität behaftet. Ein neues analytisches Modell ermöglicht es, diesen Effekt zu berücksichtigen indem das direkte und das diffuse Lichtfeld getrennt behandelt werden. Parametrisierungen für den direkten und diffusen, abwärts gerichteten Attenuationskoeffizienten, K_{dd} und K_{ds}, wurden während dieser Arbeit entwickelt. Um dies zu ermöglichen, wurden numerische Simulationen mit dem anerkannten Strahlungstransfermodel Hydrolight 5.0 durchgeführt. Das Programm wurde modifiziert, um den direkten und diffusen Anteil des Strahlungsfeldes getrennt berechnen zu können. Die neu entwickelten, analytischen Parametrisierungen wurden mit diesen Simulationen verifiziert und gegen ein kürzlich veröffentliches, semi-analytisches Modell von Pan und Zimmermann verglichen. Auch dieses Modell behandelt die direkte und diffuse Strahlung getrennt. Dessen diffuser Anteil konnte mit der entwickelten Parametrisierung für die Sonnenzenitwinkelabhängigkeit verbessert werden. Das neue analytische Model zeigt über einen großen Bereich von simulierten Wasserinhaltsstoffkonzentrationen bessere Leistungen als das originale und sogar als das verbesserte Pan-Zimmerman Modell. Die neue Parametrisierung ist nicht auf absorptionsdominierte Gewässer beschränkt. Feldmessungen wurden durchgeführt um einen Datensatz für die unabhängige Validierung des Modelles zu erstellen. Das Modell wurde an diesen Datensatz gefittet und einer der Modellparameter, die Sensortiefe, wurde gegen unabhängige Tiefenmessungen verglichen. Die Ergebnisse sind unabhängig von der Bewölkungssituation und dem Sonnenstand und zeigen sehr kleine mittlere Fehler und Standardabweichungen. Im Vergleich zu den Fitergebnissen mit dem weitverbreiteten Gordon Modell ergibt sich eine um den Faktor fünf kleinere Standardabweichung. Dies lässt auf eine erfolgreiche Berücksichtigung des 'wave-focusing' Effektes schließen. Auch die absoluten Abweichungen sind im Durchschnitt um einen Faktor drei geringer, was auf die verbesserten Parametrisierungen von K_{dd} und K_{ds} zurückzuführen ist.

Contents

List of Figures

1 Introduction

1.1 Context and Motivation

Earth remote sensing, the acquisition of spectral information about an object on the Earth surface from the distance, has grown to a mature state over the past decades. Nowadays it is not any more just an academic playground but serves society on various layers. Remote sensing has become an indispensable tool for citizens, farmers, environmentalists, politicians and decision makers, humanitarian organizations and various scientific disciplines like biology, geography, forestry, geology and oceanography.

In this work, remote sensing of water surfaces is addressed. As more than two thirds of the Earth surface are covered with water, with the vast majority far away from civilization, remote sensing plays an essential role for the investigation of oceans and lakes. The most obvious division of water covered areas is deep and shallow waters. In deep waters, such as most of the oceans and big lakes afar from shores, light cannot penetrate the water column deep enough to reach the bottom and therefore all information retrievable with remote sensing originates exclusively from the water body. In shallow waters, the bottom albedo is from importance as light reaches the ground and is reflected back to the surface. From this classification different applications automatically emerge: in deep waters, only the water composition is from interest whereas in shallow waters also information about ground cover can be evaluated.

Even though in shallow waters the information of interest normally is not about the water column, profound knowledge about the attenuation of light in water is essential to correct for the induced effects on the light field. The signal a satellite or airborne sensor receives from a water body has interacted with the water column on a scale of meters. The situation is comparable with the atmosphere, where a good correction is inevitable for any quantitative statement from the measurements. However, the main difference between the atmosphere and a water body is optical density: a satellite sensor receives most of the intensity reflected from the earth's surface whereas, even in clear waters, the vast majority of the reflected intensity originates from the first few meters in the water column. This means that only a few percent of the recorded intensities actually contain information about ground cover. The requirements for the water column correction are therefore on a very high level for shallow water spectroscopy.

The physical background of the attenuation of light in water is well understood. If the information about all water constituents is available, the correction can theoretically be considered perfect. Unfortunately, there is a large variety of parameters which influence the optical behavior of a water body. As reference field measurements are expensive and time consuming, it is a main objective to get both out of a single measurement, optical properties of the water column and information about the ground cover. To put it in mathematical means: it is a highly ambiguous problem. The best approach to such a problem is regression. Because this process is computationally very expensive, fast models are required.

The physically correct way to calculate the attenuation of light in matter is to solve the Maxwell equations, as they describe any electromagnetic field and its spacial and temporal evolution. A more specific approach offers the radiative transfer equation (RTE), which is widely accepted as a physically valid description. In atmospheric physics it is common practice to solve the RTE for inverse modeling of the atmospheric parameters. This can also be done in the case of water but due to the much higher optical density of water, at correspondingly higher computational cost.

A different approach is to use an analytical model which approximates the physical properties on a much lower level of complexity. In such a model, not the microscopical events which lead to the attenuation of light are described, but the macroscopic consequences. From the scientific point of view, a physically meaningful analytical model leads to a more intuitive and relevant understanding of the macroscopic processes than the RTE or the Maxwell equations. For the inversion of the model parameters, an analytical model offers an immense advantage in computational efficiency. The development and optimization as well as the verification of an analytical model for the attenuation of light in water is the topic of this study.

1.2 Situation

Many analytical models for the attenuation of light in water have been developed and used in remote sensing for decades. The motivation to put effort into the development of a new parameterization was based on a different problem. In order to interpret the spectra delivered by satellite or airborne sensors, reference spectra have to be collected just above and under water. As mentioned before, concerning light transfer, water behaves physically similar to air. More problematic is the air-water interface, because the analytical approximation as a perfectly flat surface, is not suitable for any realistic case; waves are always present at natural conditions. Waves can be imagined as little lenses, which focus the incoming radiation at a certain focal plane and defocus at the surrounding areas. The distance of the focal plane to the water surface is dependent on the wavelength of the water waves and therefore on various factors like wind speed and shore geometries [19]. The result of the so called

wave-focusing effect is an enormous variability of the measured under water intensities and spectral distributions. Unfortunately, this effect is even more pronounced for low wave heights [6]. The solution for this problem so far was to average over several measurements. For variabilities up to a factor of five, the measurement time necessary to obtain a statistically reliable average, is usually much longer than the time span during which constant conditions can be assumed.

The striking feature of the new analytical model which is to be optimized, is the possibility to correct for the wave-focusing effect. This is achieved by a separate treatment of direct and diffuse radiation. At each point in the water column, a certain ratio of direct to diffuse radiation is persistent, which can be influenced by the wave-focusing effect. The fractions differ in spectral shape which is exploited in the regression of the model to determine the actual composition of direct to diffuse radiation for each measurement. The other model parameters therefore become independent of this ratio and the effects induced by wave-focusing.

As the new model treats direct and diffuse radiation completely separate, the attenuation behavior has to be characterized independently. The model parameter responsible for this is the downwelling attenuation coefficient K_d. As this approach hasn't been followed ever before, existing models for K_d only describe the attenuation behavior for the complete radiation. Therefore two independent parameterizations for K_d have to be developed for the new model: K_dd for the direct and K_ds for the diffuse radiation.

1.3 Approach

As mentioned before, the RTE in water can be solved numerically. The most widely used program for this matter is called Hydrolight by Curtis Mobley and Lydia Sundman [15]. In order to simulate in-water radiation separately for the direct and diffuse component, Hydrolight was modified accordingly during this study, as described in chapter 4. The results were used to develop two independent parameterizations for the attenuation coefficients of direct and diffuse irradiance[1] in water. The new model, in combination with the developed parameterizations for K_dd and K_ds, was verified against the numeric simulations. To have an independent verification of the model's performance, field measurements were carried out under various conditions, concerning sun zenith angle, geometrical depth and cloud cover, as described in chapter 5. These measurements were fitted to the newly developed model with the public domain software WASI [5]. One fitted model parameter, the sensor depth, was compared to independent measurements. The new model is expected to increase the accuracy of the sensor depth fit, compared to prevailing models for downwelling irradiance attenuation.

[1] irradiance: a specific measure for radiation. For the definition, see chapter 2.

Also the variability of the fit results for the sensor depth should be significantly lower, as the wave-focusing effect can be corrected for in the new model.

2 Theoretical Background

The aim of this work is to describe how light is being influenced as it propagates through water. Therefore it is necessary to define the quantities which characterize the light field and the influence of water to them. In this chapter an introduction to the theoretical background of this work is given. First some fundamental equations and definitions concerning light and its attenuation in water are explained, followed by a short overview of some of the existing analytical models.

2.1 Fundamentals

2.1.1 Radiance and Irradiance

A light field can be described by a quantity called *unpolarized spectral radiance* L or in the following briefly *radiance*.

$$L(\mathbf{x}, t, \phi, \theta, \lambda) = \frac{\Delta Q}{\Delta t \Delta A \Delta \Omega \Delta \lambda} \qquad [\mathrm{Wm^{-2}sr^{-1}nm^{-1}}] \tag{2.1}$$

This definition gives the radiance at a certain point in time (t) and space ($\mathbf{x}$) at a wavelength λ resulting from the radiant energy ΔQ which is collected in an area ΔA over the intervals

- Δt in time (centered at time t)
- $\Delta\Omega$ in solid angle (centered at direction (ϕ/θ)[1])
- $\Delta\lambda$ in wavelength (centered at wavelength λ)

If one is not interested in the angular distribution of the light field there are many quantities to be used which mainly differ by the way they weight radiance from different directions. For the purposes of this study, the *spectral downwelling plane irradiance* E_d, in the following abbreviated with *downwelling irradiance* or just *irradiance*, is used.

$$E_{\mathrm{d}}(\mathbf{x}, t, \lambda) = \frac{\Delta Q}{\Delta t \Delta A \Delta \lambda} \qquad [\mathrm{Wm^{-2}nm^{-1}}] \tag{2.2}$$

[1] ϕ : azimuth angle, θ: zenith angle

For this quantity it is assumed that every point on a fictive detector's flat surface is equally sensitive to incoming radiant energy, no matter which direction it originates from. However, as the detector's area is a flat surface, a beam originating from an angle different to zenith will always illuminate an effective surface area which is increased by a factor of $\cos\theta$, where θ is the angle to the instrument's optical axis. For that reason this kind of detector is called a *cosine collector*.

The relation between *radiance* and *downwelling irradiance* is therefore the integral over the upper half space ($\Omega_{up}(\theta, \phi)$, θ: zenith, ϕ: azimuth), weighted with the factor $\cos\theta$.

$$E_\mathrm{d}(\mathbf{x}, t, \lambda) = \int_{\Omega_{up}} L(\mathbf{x}, t, \phi, \theta, \lambda)\, |\cos\theta|\, \mathrm{d}\Omega \tag{2.3}$$

$$= \int_{\phi=0}^{2\pi} \int_{\theta=0}^{\pi/2} L(\mathbf{x}, t, \phi, \theta, \lambda)\, |\cos\theta|\, \sin\theta\, \mathrm{d}\phi\, \mathrm{d}\theta \tag{2.4}$$

Another way to weight the incoming radiance is the *spectral downwelling scalar irradiance* which is collected not by a flat surface but a half-sphere shaped detector. Therefore a detector for this quantity is called *2π collector*.

$$E_{0\mathrm{d}}(\mathbf{x}, t, \lambda) = \int_{\Omega_{up}} L(\mathbf{x}, t, \phi, \theta, \lambda)\, \mathrm{d}\Omega(\theta, \phi) \tag{2.5}$$

$$= \int_{\phi=0}^{2\pi} \int_{\theta=0}^{\pi/2} L(\mathbf{x}, t, \phi, \theta, \lambda)\, \sin\theta\, \mathrm{d}\phi\, \mathrm{d}\theta \tag{2.6}$$

2.1.2 Exponential Decay with Depth

According to the *Lambert-Beer Law*, underwater *downwelling irradiance* E_d decays roughly exponential with depth [13]:

$$E_\mathrm{d}(\lambda, z) = E_\mathrm{d}(\lambda, 0^-) \cdot \exp(-\overline{K}_d \cdot z). \tag{2.7}$$

Relation 2.7 extrapolates the *downwelling irradiance* E_d just beneath the water surface ($z = 0^-$) to values of E_d for increasing depths. This simple approach is very useful as the exponent $\overline{K}_\mathrm{d}$ is, as a first approximation, only dependent on the wavelength. For a plot of $\ln(E_\mathrm{d})$ against depth, a linear relationship is expected. This is shown in the right panel of figure 2.1.

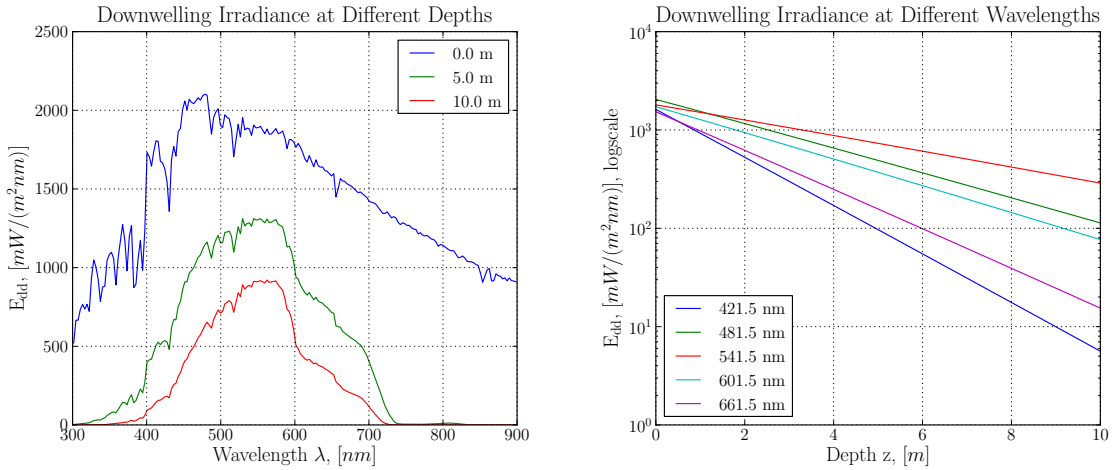

Figure 2.1: Downwelling irradiance at different depths and wavelengths, calculated with parameter set 1 from section 4.3.

2.2 Spectral Downwelling Diffuse Attenuation Coefficient K_d

The spectral downwelling diffuse attenuation coefficient K_d is the quantity which describes the attenuation behavior of E_d. It is is defined as follows [13]:

$$\begin{aligned} K_d(\lambda, z) &= -\frac{d \ln E_d(\lambda, z)}{dz} \\ &= -\frac{1}{E_d(\lambda, z)} \frac{dE_d(\lambda, z)}{dz} \end{aligned} \tag{2.8}$$

As the attenuation behavior of E_d is actually not perfectly exponential, K_d is still slightly dependent on depth. Therefore the relevant quantity to estimate E_d at a certain depth is the average K_d from just below the surface to a given depth:

$$\overline{K}_d(\lambda, z) = \frac{1}{z} \int_0^z K_d(\lambda, z') dz' \tag{2.9}$$

The wavelength dependency of the attenuation due to absorption and scattering is the most important factor for an analytical description of K_d. In a next step the influence of the sun zenith angle, the scattering phase function and the change of the under water light field with depth are to be taken into account.

2.2.1 Absorption

The process of absorption converts energy in form of a radiant flux (photons) to other forms of energy, e.g. thermal or chemical energy. It is defined as [3]:

$$a = -\frac{\mathrm{d}\Phi_a}{\Phi \cdot \mathrm{d}r} \tag{2.10}$$

Where $\mathrm{d}\Phi_a$ is the absorbed part of the original radiant flux Φ over an infinitesimal distance $\mathrm{d}r$. In typical natural water bodies the total absorption is composed of pure water, chlorophyll and yellow substance absorption in a range of 0-3 m^{-1} at wavelengths between 400 and 800 nm.

2.2.2 Scattering

The second important factor for attenuation of light in water is scattering. In water, scattering is mainly elastic: photons are only deviated from the original path and their energy is conserved. Inelastic scattering, in the form of Raman scattering or fluorescence, is normally of rather small importance. The *volume scattering function* (VSF, $\beta(\theta, \phi)$) of a certain substance describes its angular dependency and magnitude of scattering. The integral over the VSF and the full space is the *scattering coefficient* b which equals the total amount of scattering in any direction for the given substance (and concentration). The dependence of scattering on the scattering angle is described by the scatterer's *phase function* $\tilde{\beta}(\theta, \phi)$ which describes the scattering probability for an incoming photon into any direction (θ, ϕ). As it is a probability distribution function its integral over the whole space (Ω) is equal to one. The phase function is not dependent on the concentration of the scattering substance.

$$\begin{aligned} \beta(\theta, \phi) &= -\frac{\mathrm{d}\Phi_s(\theta, \phi)}{\Phi \cdot \mathrm{d}r \cdot \mathrm{d}\Omega} \\ \tilde{\beta}(\theta, \phi) &= \beta(\theta, \phi)/b \\ b &= \iint_{\Omega} \beta(\theta, \phi)\, \mathrm{d}\Omega \end{aligned} \tag{2.11}$$

Where $\mathrm{d}\Phi_s$ is the scattered part of the original radiant flux Φ (into direction (θ, ϕ)) over an infinitesimal distance $\mathrm{d}r$ and solid angle $\mathrm{d}\Omega$. If one is interested in the scattered radiant flux in the lower (Ω_{down}) or upper half-space (Ω_{up}) the corresponding scattering coefficients can

be calculated as follows:

$$\begin{aligned} b_\mathrm{f} &= \iint\limits_{\Omega_\mathrm{down}} \beta(\phi,\theta)\,\mathrm{d}\Omega(\theta,\phi) = 2\pi \cdot \int\limits_{0}^{\pi/2} \beta(\theta)\,\sin(\theta)\,\mathrm{d}\theta \\ b_\mathrm{b} &= \iint\limits_{\Omega_\mathrm{up}} \beta(\phi,\theta)\,\mathrm{d}\Omega(\theta,\phi) = 2\pi \cdot \int\limits_{\pi/2}^{\pi} \beta(\theta)\,\sin(\theta)\,\mathrm{d}\theta \\ b &= b_\mathrm{f} + b_\mathrm{b} \end{aligned} \tag{2.12}$$

Here, the VSF is assumed to be symmetrical to the direction of photon traveling and therefore invariant with respect to ϕ [4] (the integration over ϕ results in a factor 2π). The integration limits due to the definition of the upper and lower half spheres Ω_{up} and Ω_{down} are drawn in figure 2.2. Typical spectra for absorption, scattering and backscattering coefficients are plotted in figure 4.1 of chapter 4.

2.2.3 Sun Zenith Angle θ_sun

The attenuation in the water column through absorption and scattering is dependent on the geometrical path length. A ray of light, coming from a non-zenith position θ, will have a longer path in the water column than the geometrical depth. From geometrical considerations this dependency can be accounted for with a factor of $\cos(\theta^\mathrm{w}_\mathrm{sun})^{-1}$ (where $\theta^\mathrm{w}_\mathrm{sun}$ is the sun zenith angle below the water surface calculated with Snell's law[2]). However, this correction is only strictly valid for photons which haven't been deviated on their way from the sun disc through the atmosphere and the water column. This is the case for the majority of photons in the atmosphere, at least on a sunny and cloud free day. However, diffuse illumination is always present due to scattering in the atmosphere. In the water column, scattering processes lead to a increasingly diffuse light field distribution with depth.

2.2.4 Sun Zenith Angle Dependent Backscattering Coefficient

In equations 2.12, the VSF is used to calculate the back- and forward scattering coefficients. The backscattering coefficient b_b is used in most present K_d models, though it is valid only for the sun at zenith position. With the knowledge of the constituents' VSFs, the model results can be easily improved by calculating the sun zenith angle dependent backscattering coefficient, denoted as $b_\mathrm{b}(\theta^\mathrm{w}_\mathrm{sun})$. The effect of this correction is shown in chapter 6.

[2] $\sin(\theta^\mathrm{w}) = \frac{\sin(\theta)}{n}$, $n = 1.34$: refractive index of sea water [13]

The scattering constituents in typical waters are the water itself and suspended matter. The VSF for water is very similar to Rayleigh scattering (which is scattering of light by particles much smaller than the wavelength of the light):

$$\beta_{\mathrm{w}}(\theta,\lambda) = \beta_{\mathrm{w}}(90°,\lambda_0)\cdot\left(\frac{\lambda_0}{\lambda}\right)^{4.32}\cdot(1+0.835\cos^2\theta) \tag{2.13}$$

With $\beta_{\mathrm{w}}(90°,\lambda_0) = 8.9946\ \mathrm{m^{-1}sr^{-1}}, \lambda_0 = 350$ nm [13] (Valid for sea water, $\beta_{\mathrm{w}}(90°,\lambda_0)$ marginally corrected to fit Hydrolight values, see chapter 4).

In the case of suspended matter, concentration needs to be accounted for and thus the phase function, rather than the VSF, is used. The phase function which is most widely used for suspended matter is the *Petzold San Diego Harbor* [18] phase function. It is quite elaborate to measure the phase function of a specific suspended matter composition and it was shown [13] that there isn't much variation over typical waters of interest. Thus Petzold measurements are widely accepted as a representative phase function for suspended matter. The main feature is a strong peak in the forward direction and a relatively small and constant fraction of backscattering (see [14], Fig. 1). There are many approaches to an analytical description of the average Petzold phase function[3] which are extensively compared in [14] and the Fournier-Forand phase function ($\tilde{\beta}_{ff}(\theta)$) turned out to be the best choice. It is also the phase function which is implemented into Hydrolight [15]. Details on the actual implementation can be found in [14].

With the knowledge of the VSF of water, the phase function of suspended matter and its scattering coefficient $b^{\mathrm{sm}}(\lambda)$ it is possible to calculate a sun zenith angle dependent backscattering coefficient for a given water body. The direction of the incident direct radiation might be tilted with respect to the zenith position by the angle θ_{sun} and therefore also the phase function relative to the water body (fig. 2.2). Similar to b_{b}, the fraction of light scattered in the upper half sphere is from interest. The integral limits have to be adjusted to represent the upper half sphere in the tilted phase function coordinate system:

$$\begin{aligned} b_{\mathrm{b}}^{\mathrm{w}}(\theta_{\mathrm{sun}}^{\mathrm{w}},\lambda) &= \pi\cdot\int_{\frac{\pi}{2}-\theta_{\mathrm{sun}}^{\mathrm{w}}}^{\frac{3}{2}\pi-\theta_{\mathrm{sun}}^{\mathrm{w}}}\beta_{\mathrm{w}}(\theta,\lambda)\ |\sin\theta|\ \mathrm{d}\theta \\ b_{\mathrm{b}}^{\mathrm{sm}}(\theta_{\mathrm{sun}}^{\mathrm{w}}) &= \pi\cdot\int_{\frac{\pi}{2}-\theta_{\mathrm{sun}}^{\mathrm{w}}}^{\frac{3}{2}\pi-\theta_{\mathrm{sun}}^{\mathrm{w}}}\tilde{\beta}_{\mathrm{ff}}(\theta)\ |\sin\theta|\ \mathrm{d}\theta\cdot b^{\mathrm{SM}}(\lambda). \end{aligned} \tag{2.14}$$

[3] Petzold measured waters of different turbidity and composition. Most analytical models average over all of those phase functions and name it 'average Petzold phase function'.

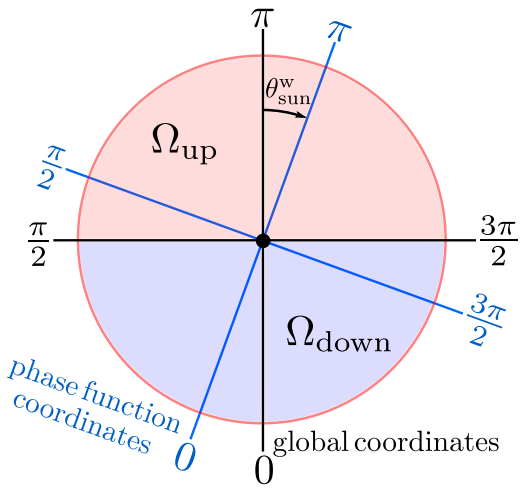

Figure 2.2: Global coordinate system and phase function coordinate system, tilted by $\theta^\mathrm{w}_\mathrm{sun}$. For the calculation of $b^\mathrm{w}_\mathrm{b}(\theta^\mathrm{w}_\mathrm{sun})$, the phase function has to be integrated in its coordinate system over the upper half sphere Ω_up.

The integration over the full upper half sphere is necessary to preserve symmetry and is compensated with a factor $\frac{1}{2}$. As the integrand would render negative values for zenith angles above π, the absolute values of $\sin(\theta)$ are used for the calculation. The resulting backscattering coefficient is then just the sum of the two contributing scatterers:

$$b_\mathrm{b}(\lambda, \theta^\mathrm{w}_\mathrm{sun}) \quad = \quad b^\mathrm{w}_\mathrm{b}(\lambda, \theta^\mathrm{w}_\mathrm{sun}) + b^\mathrm{sm}_\mathrm{b}(\theta^\mathrm{w}_\mathrm{sun}). \tag{2.15}$$

For $\theta^\mathrm{w}_\mathrm{sun} = 0°$, the parameter b_b equals $b_\mathrm{b}(\theta^\mathrm{w}_\mathrm{sun})$. In figure 2.3, $b_\mathrm{b}(\lambda = 450\,\mathrm{nm}, \theta^\mathrm{w}_\mathrm{sun})$ is plotted for sun zenith angles in a range of 0° to 90° for all parameter sets, as defined in section 4.3. For the parameterizations in chapter 6 the sun zenith angle averaged backscattering coefficient is necessary:

$$\overline{b_\mathrm{b}}(\lambda) = \int_0^{\theta^\mathrm{w}_\mathrm{sun}(\pi)} b_\mathrm{b}(\lambda, \theta^\mathrm{w}_\mathrm{sun})\,\mathrm{d}\theta^\mathrm{w}_\mathrm{sun}, \tag{2.16}$$

with $\theta^\mathrm{w}_\mathrm{sun}(\theta_\mathrm{sun})$ calculated with Snell's law, as mentioned above. As performance is one main advantage of an analytical solution for $\overline{K}_\mathrm{dd}$ and $\overline{K}_\mathrm{ds}$, a numerically efficient parameterization for equation 2.16 is desired. The concentration and wavelength dependencies of the integrals can be separated. The remaining integrals ($\overline{\beta_\mathrm{w}}$, $\overline{\tilde{\beta}_\mathrm{SM}}$) are only dependent on the sun zenith angle and were solved numerically. Thus the average sun zenith angle dependent

backscattering coefficient can be parameterized as follows:

$$\overline{b_\mathrm{b}}(\lambda) = \beta_\mathrm{w}(90°, \lambda_0) \cdot \left(\frac{\lambda_0}{\lambda}\right)^{4.32} \cdot \overline{\beta_\mathrm{w}} + \left(\frac{b_\mathrm{b}^\mathrm{SM}}{b^\mathrm{SM}}\right)^{-1} \cdot C_\mathrm{SM} \cdot b_\mathrm{b}^{\mathrm{SM}*} \cdot \overline{\tilde{\beta}_\mathrm{SM}}, \tag{2.17}$$

with $\beta_\mathrm{w}(90°, \lambda_0) = 0.000138\ \mathrm{m^{-1}sr^{-1}}$, $\lambda_0 = 500$ nm, $\overline{\beta_\mathrm{w}} = 2.557$, $\overline{\tilde{\beta}_\mathrm{SM}} = 0.00871$ and $\frac{b_\mathrm{b}^\mathrm{SM}}{b^\mathrm{SM}}$ for the backscattering to scattering ratio of suspended matter, which was approximated in this study with 0.0191. C_SM is the suspended matter concentration and $b_\mathrm{b}^{\mathrm{SM}*}$ its specific backscattering coefficient with a value of $0.0086\ \mathrm{m^2g^{-1}}$ [5]. The inverse calculations in this study were carried out with WASI, as described in section 5.6. Equation 2.17 was used for this purpose.

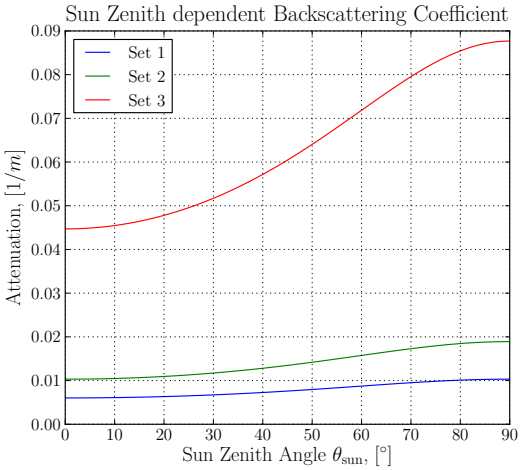

Figure 2.3: Sun zenith angle dependent backscattering coefficient at a wavelength of 450 nm calculated with all parameter sets from section 4.3.

2.2.5 Depth z

K_d is also weakly dependent on depth. As mentioned above, the reason for this is the change of the underwater light field distribution through scattering. Light becomes increasingly diffuse with depth, until all direct light from the sun has been scattered out of its original direction. The result is that K_d slowly changes with depth, from its values just below the surface, to a certain value $K_\mathrm{d}(\infty)$ which is not dependent on depth anymore.

This change in light field distribution can be expressed with the *downwelling mean cosine* $\overline{\mu}_\mathrm{d} = \frac{E_\mathrm{d}}{E_\mathrm{0d}}$. It describes the change of the downwelling light field with depth and could therefore be used to correct K_d values accordingly. Unfortunately, there exists no analytical approximation which could be exploited. However, as E_d and E_0d are normally part of numerical simulations, $\overline{\mu}_\mathrm{d}$ can be used as an approximation for the best result which can be

achieved with analytical K_d-models, e.g.:

$$E_\mathrm{d}(\lambda, z, \theta^\mathrm{w}_\mathrm{sun}) \approx E_\mathrm{d}(\lambda, 0^-, 0) \cdot \exp\left[-(a + b_\mathrm{b}) \cdot \left[\int_0^z \overline{\mu}_\mathrm{d}(\lambda, z', \theta^\mathrm{w}_\mathrm{sun})\mathrm{d}z'\right]^{-1}\right]. \quad (2.18)$$

2.3 Existing Parameterizations of K_d

With the perception that absorption and scattering must be the only reasons for attenuation of light in water, the first analytical models for K_d became possible. One important step in the parameterization of K_d was first implemented by Gordon[1975] [8]: the assumption that the relevant part of scattering for attenuation is backscattering - scattering into the upper half space (because light which is scattered to forward directions is still a part of the downwelling light field). The sun zenith dependency was accounted for by the *downwelling average cosine* $\overline{\mu}_0 = \cos\theta^\mathrm{w}_\mathrm{sun}$ which is only valid for a black sky without atmosphere (no diffuse light due to scattering). This factor just corrects for the longer path length, compared to the geometrical depth, of direct radiation through the water column. Because diffuse radiation cannot be accounted for in this way (as it originates from any direction), Gordon corrected his model with an empirical factor $\kappa_0 = 1.0395$:

$$K_d = \frac{\kappa_0 \cdot (a + b_\mathrm{b})}{\overline{\mu}_0}. \quad (2.19)$$

κ_0 can be understood as a mean path prolongation factor due to the diffuse light field. Gordon[1989] [7] introduced a normalization factor D_0 which improves the sun zenith angle dependency approximation (it corrects for the influence of incident diffuse light). For the correction it is necessary to measure the direct and diffuse parts of the incident light field separately (e.g. by shading the sensor):

$$\begin{aligned} K_d &= \kappa_0 \cdot (a + b_\mathrm{b}) \cdot D_0, \quad (2.20)\\ D_0 &= \frac{f}{\overline{\mu}_0} + 1.197 \cdot (1 - f),\\ f &= \frac{E_\mathrm{d}(\mathrm{direct})}{E_\mathrm{d}(\mathrm{direct}) + E_\mathrm{d}(\mathrm{diffuse})}. \end{aligned}$$

The fact that K_d slowly varies with depth is neglected in this model. A slightly different approach is the one of Kirk[1991] [11] for an average value of K_d over the euphotic zone[4], $\overline{K}_\mathrm{d}$:

$$\begin{aligned} \overline{K}_\mathrm{d} &= \frac{(a^2 + G \cdot a \cdot b)^{\frac{1}{2}}}{\overline{\mu}_0}, \\ G(1\,\%) &= 0.425 \cdot \overline{\mu}_0 - 0.19, \\ G(10\,\%) &= 0.473 \cdot \overline{\mu}_0 - 0.218. \end{aligned} \tag{2.21}$$

The parameters $G(1\,\%)$ and $G(10\,\%)$ are to be chosen to calculate the average K_d down to the 1 % or 10 % surface irradiance level, respectively. Still, this approach didn't provide a depth dependency and leaves remaining dependencies concerning the VSF of the parameter G unexplained. One of the first depth-dependent models was presented by Bannister[1992] [2]. His model interpolates between the K_d-values just below the surface and an asymptotic value for infinitely deep water with an exponential function. Unfortunately the model rendered reasonable results only for sun zenith angles less than 48°. The semi-analytical approach of Lee[2005] [12] is based on the radiative transfer equation:

$$K_\mathrm{d}(z) = m_0(z, \theta_\mathrm{sun}) \cdot a + \nu(z, \theta_\mathrm{sun}) \cdot b_\mathrm{b}. \tag{2.22}$$

In the model, absorption and backscattering are treated by individual parameters m_0 and ν. The dependencies of those two parameters are not described by analytical expressions but stored in look-up tables. Because the parameters are derived from numerical simulations which were carried out for specific water compositions, the model cannot claim to be universally valid. Recently, Pan and Zimmerman[2010] [17] presented a new model concerning K_d. To the author's knowledge, it is the first published model for K_d, which treats direct and diffuse radiation separately.

$$\begin{aligned} \overline{K}_\mathrm{d}^\mathrm{direct} &= \frac{1}{\overline{\mu}_0}\left[K_\mathrm{d}(\infty) + \frac{[a + b_\mathrm{b} - K_\mathrm{d}(\infty)]}{Pcz} \cdot [1 - \exp(-Pcz)]\right] \\ K_\mathrm{d}^\mathrm{diffuse} &= (1.317 - A_0\omega_0 - A_1\omega_0^2) \cdot c \\ \omega_0 &= \frac{b}{c} \\ c &= a + b \end{aligned} \tag{2.23}$$

The parameters $K_\mathrm{d}(\infty), P, A_0, A_1$ are functions of the backscattering ratio $\frac{b_\mathrm{b}}{b}$ and ω_0. The fraction direct to diffuse solar irradiance is described by an exponential function of wavelength. The parameterization of $\overline{K}_\mathrm{d}^{direct}$ bears resemblance to the model of Bannister[1992] as it also interpolates between the K_d-value below the surface and the asymptotic value for infinitely deep water with an exponential function. The parameterization of the diffuse K_d inherits no

[4]The euphotic zone ends where the intensity has reached the 10% or 1% level compared to the value just below the water surface, depending on the definition.

depth or sun zenith dependency. This is most likely due to the fact that the authors couldn't numerically simulate diffuse irradiances and therefore had to rely on a simulation at 89° sun zenith angle as a quasi-diffuse approximation. As simulations for diffuse irradiances also at varying sun zenith angles could be performed in this study, an improved parameterization for the diffuse K_d of the Pan-Zimmerman model was developed and included in the comparison. In chapter 6 the model is used as a reference for the comparison with the newly developed parameterizations.

3 The Analytical Model

Most authors of existing under water irradiance models are aware of the fact that the direct and diffuse components of the light field have different behaviors, which needs to be accounted for (e.g. Gordon[1975] introduced his empirical factor κ_0 in equation (2.19)). The first model, which actually treats those two components strictly separate is the one of Gege[2011] [6]. The different spectral shapes of E_{dd} and E_{ds} are exploited to separate them from each other. The principle idea is that each E_{d}-spectrum is the weighted sum of a direct and a diffuse component:

$$E_{\mathrm{d}} = f_{\mathrm{dd}} E_{\mathrm{dd}} + f_{\mathrm{ds}} E_{\mathrm{ds}}. \tag{3.1}$$

The weighting factors f_{dd} and f_{ds} are equal to one for a cloudless reference atmosphere and unobscured sky view[1]. Under water, this remains true for a completely plane water surface. As surface waves are basically always present for any in situ measurement, the intensities of the direct and diffuse irradiances are altered by the wave focusing effect [19]. The waves act like lenses on the water surface: they focus incoming light to a certain focal distance in the water column. As a result, the intensity increases at this point which is reflected by a factor f_{dd} or $f_{\mathrm{ds}} > 1$. Reversely, defocussing leads to lower intensities (f_{dd} or $f_{\mathrm{ds}} < 1$). The focal distance is dependent on the wavelength of the surface waves. The effect is even more pronounced for calm conditions [19], which makes a correction for the wave focusing effect indispensable.

As water waves are not static in size or wavelength, the resulting under water light field is highly variable. The effect is most pronounced at relatively calm water surfaces and clear skies, leading to typical variabilities in E_{d} of 20 - 40 % near the water surface. However, flashes of focused light can lead to intensity changes up to a factor of five (see figure 3.2 and [6]). It is important to understand that this effect influences direct and diffuse irradiance in the same way. Though the direct component leads to the highest variabilities as its spacial distribution is highly peaked at the sun disc's position. The diffuse light field is quite homogeneously distributed over the complete sky[2] and therefore the wave-focusing effect does not lead to a focus at a distinct plane. As both components are different in spectral shape (figure 3.1), it

[1] as defined in Gregg&Carder[1990] [9]

[2] more exactly: it can be approximated as cardiodal [10]

is possible to fit equation 3.1 to a given under water spectrum and determine f_{dd} and f_{ds}. The separation makes the fit independent from the wave situation on the water surface at the time of the measurement. With this approach it is not necessary to average over a large number of measurements, as it used to be done to account for the high variability in E_{d}.

The reasons of attenuation with depth are the same for E_{dd} and E_{ds}: absorption and scattering. However, both components differ in spectral shape and spacial distribution. With the new model it is possible to account for those differences. The assumption of exponential decrease is still valid for both, but the attenuation coefficients K_{dd}, K_{ds} can be treated individually:

$$\begin{aligned} E_{\mathrm{dd}}(\lambda, z) &= E_{\mathrm{dd}}(\lambda, 0^-) \cdot \exp(-\overline{K}_{\mathrm{dd}} \cdot z) \\ E_{\mathrm{ds}}(\lambda, z) &= E_{\mathrm{ds}}(\lambda, 0^-) \cdot \exp(-\overline{K}_{\mathrm{ds}} \cdot z), \end{aligned} \tag{3.2}$$

where the bars in $\overline{K}_{\mathrm{dd}}, \overline{K}_{\mathrm{ds}}$ indicate depth averages, as defined in eqation (2.9). To optimize the parameterization for $\overline{K}_{\mathrm{dd}}$ and $\overline{K}_{\mathrm{ds}}$, given in [6][3]:

$$\begin{aligned} \overline{K}_{\mathrm{dd}} &= (a + b_{\mathrm{b}}) \cdot \left(\cos\theta'_{\mathrm{sun}}\right)^{-1} \\ \overline{K}_{\mathrm{ds}} &= (a + b_{\mathrm{b}}) \cdot l_{\mathrm{ds}} \\ l_{\mathrm{ds}} &= 1.18 \pm 0.05, \end{aligned} \tag{3.3}$$

was a main goal of this work. Because (3.2) is an exponential law, an error in the average attenuation coefficient ($\Delta\overline{K}_{\mathrm{d}}$) affects the relative error of the calculated irradiance linearly with depth:

$$\frac{\Delta E_{\mathrm{d}}}{E_{\mathrm{d}}} = \frac{\partial E_{\mathrm{d}}}{\partial \overline{K}_{\mathrm{d}}} \cdot \Delta\overline{K}_{\mathrm{d}} \cdot E_{\mathrm{d}}^{-1} = z \cdot \Delta\overline{K}_{\mathrm{d}}. \tag{3.4}$$

The same argumentation holds for the inversion, but leading to errors in the fit parameters. An inversion of equation 3.1 results in an estimation for the model parameters a, b_{b} and sensor depth. The sensor depth is important for the water column correction. The absorption and backscattering coefficients contain information about the water constituent concentrations, which are also from great interest. A good parameterization for K_{dd} and K_{ds} is therefore essential for the use of such an analytical model.

[3] the notation for the Gege-Pinnel model in this work differs slightly from the one used in [6]: the path length correction for the direct component is included in the K_{dd} parameterization instead of the E_{dd} exponent.

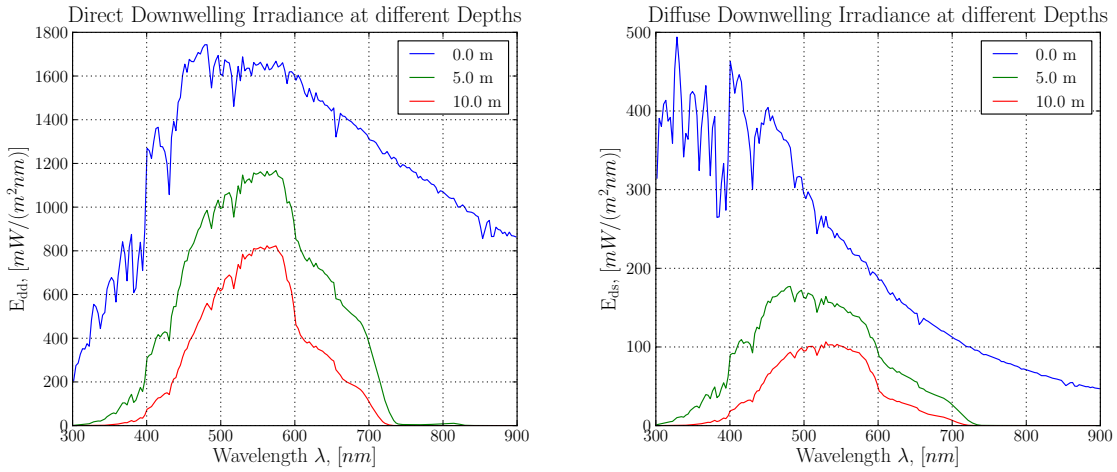

Figure 3.1: Different in shape: direct and diffuse downwelling irradiance at different depths and wavelengths. Calculcated with parameter set 1, section 4.3.

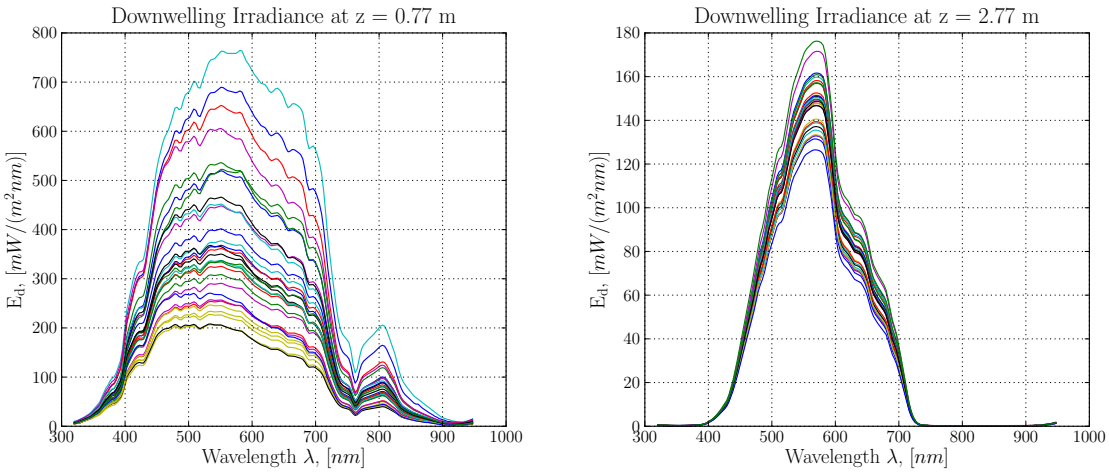

Figure 3.2: High variability: downwelling irradiance measured at 0.77 and 2.77 m (left, right) over a period of six minutes. Field measurement dataset M1 (calm conditions), table 5.1.

4 Simulations

4.1 Hydro-/Ecolight

Hydrolight [15] is a numerical solver for the time-independent radiative transfer equation (RTE). The calculated quantity is the radiance distribution within and leaving a plane-parallel water body. As the radiance is the fundamental quantity in radiometry, all other quantities from interest can be calculated from it. The program uses the mathematical technique of invariant embedding to solve the RTE. In comparison to other methods, such as Monte Carlo simulations and discrete ordinates, invariant embedding allows to perform calculations in a vertically stratified water column without performance deficits, in comparison to the homogeneous case. The approximation of a water body as plane-parallel reduces the calculations to a one-dimensional problem.

The input parameter expected by Hydrolight are the inherent optical properties[1] of the water body and the spectral sky radiance distribution. Capillary wave slope statistics (Cox-Munk) can be used to simulate a wind-blown sea surface. A bottom boundary layer can be defined for the simulations of shallow waters.

The directional radiance dependency is partitioned into 'quads'. A quad is a patch of the unit sphere bounded by circular arcs of constant polar or azimuthal angle, respectively. In Hydrolight, the complete unit sphere is divided into $10^\circ \times 15^\circ$ quads and two polar caps. Within these quads, the angular dependency of the calculated radiances is averaged. A derivation from Hydrolight, Ecolight, was developed to speed up the calculations in situations where the azimuth dependency is not from importance, as it was the case in this study. Consequently, a quad in Ecolight is rather a slice, bounded by arcs of constant polar angles. The standard polar angle resolution used by Ecolight is 10°. This resolution turned out to be not sufficient for the study of the solar zenith angle dependency, as discussed in section 4.5. Hence, a 2° discretization was used for parts of the calculations in this study.

[1] IOPs: absorption and scattering coefficients and scattering phase functions.

4.2 Modifications on Ecolight

In order to examine the distinct behavior of the direct and diffuse light field it was necessary to modify Hydro-/Ecolight in a way to differentiate between the two parts. The first approach was to adjust the illumination conditions so that either a sun in a black sky (no diffuse radiation) or a completely overcast sky (no direct radiation) is calculated. But since a change in the atmospheric parameters is necessary to do so, not the same physical setup is used for both calculations.

The second approach was geometric: Hydolight defines the light which originates from the quad where the sun is located, as direct radiation. If that quad is left out, the light field is purely diffuse. For this study, this was also not promising as Ecolight is used (radiances were of no interest) for the calculations. Ecolight does not divide the sky into quads but 'slices', as explained above. If the sun-containing slice is left out, also a significant part of diffuse radiation is neglected.

The sky-radiance model used in Hydro-/Ecolight is the one from Gregg&Carder [9]. The model already treats the direct and diffuse light field distinctly but Hydro-/Ecolight adds together the two components before proceeding to the calculations under water. If only one component of the calculated above-water light field enters the water column, its behavior can be studied independently.

Therefore the Gregg&Carder implementation in Hydro-/Ecolight was modified in this way and a new parameter was added to the runfiles of Hydro-/Ecolight to set the incident atmospheric radiation to a certain component:

- 0: calculations with mixed components (normal behavior)
- 1: calculations with the diffuse component
- 2: calculations with the direct component

The sum of the two separately calculated components equals the mixed components solution, which was verified for all calculated parameter sets. The modification doesn't prevent direct light to be scattered in the water column and therefore become diffuse (as not from the sun disc's position). The separation of direct and diffuse radiation in the new analytical model (chapter 3) is done by exploiting their different spectral shapes. From this point of view, the modification of Ecolight enables the calculation of a purely direct or diffuse light field. However, a doubled computational time has to be taken into account.

4.3 Parameters

The 4-component model of Hydro-/Ecolight for case-2 waters is used for this study with three parameter sets of different constituent concentrations (table 4.1) to cover a wide range of absorption and scattering values (table 4.2). The concentrations of set 1 resembles the concentrations of the water bodies measured in-situ during this study (chapter 5). Set 2 is an intermediate case between absorption dominated set 1 and scattering dominated set 3. The simulations are carried out in a wavelength range of 300-900 nm in steps of 3 nm. As explained in section 4.5, only the values at wavelengths between 400 nm and 830 nm are used for the final analysis. No internal sources or inelastic scatterers are assumed and the distance to the bottom is set to infinity. The contributions of the water constituents to the total absorption and scattering coefficients are plotted in figure 4.1 for all parameter sets. The refractive index of water is set to 1.34. The spectra for pure water absorption and scattering and the chlorophyll absorption are imported from WASI [5]. The yellow substance exponent is set to 0.014.

Table 4.1: Used water constituent concentrations

Component	Set 1	Set 2	Set 3
Chlorophyl (CHL), [mg m^{-3}]	2.0	1.0	0.1
Yellow substance (Y), [m^{-1}]	0.35	1.0	0.1
Suspended matter (SM), [g m^{-3}]	0.5	1.0	5.0

Table 4.2: Range of absorption und scattering coefficients for all water constituent concentrations calculated in the wavelength range 400-830 nm.

	$[1/m]$	a	a_{water}	a_{CHL}	a_{Y}	b	b_{water}	b_{SM}	b_{b}/b, $[-]$
Set 1	min	0.1582	0.0058	0.0000	0.0015	0.2252	0.0002	0.2250	0.0196
	max	3.1790	3.1775	0.0678	0.6085	0.2308	0.0058	0.2250	0.0312
Set 2	min	0.2464	0.0058	0.0000	0.0043	0.4502	0.0002	0.4500	0.0194
	max	3.1817	3.1775	0.0339	1.7385	0.4558	0.0058	0.4500	0.0252
Set 3	min	0.0690	0.0058	0.0000	0.0004	2.2503	0.0002	2.2500	0.0192
	max	3.1779	3.1775	0.0034	0.1738	2.2558	0.0058	2.2500	0.0203
Absolute	min	0.0690	0.0058	0.0000	0.0004	0.2252	0.0002	0.2250	0.0192
	max	3.1817	3.1775	0.0678	1.7385	2.2558	0.0058	2.2500	0.0312

The atmospheric conditions were chosen as follows:

- Windspeed: 0 km/h
- Sun zenith angle: 0 - 80°, 1° steps
- Cloud cover: 0 %
- Pressure: 101.325 kPa (standard conditions)

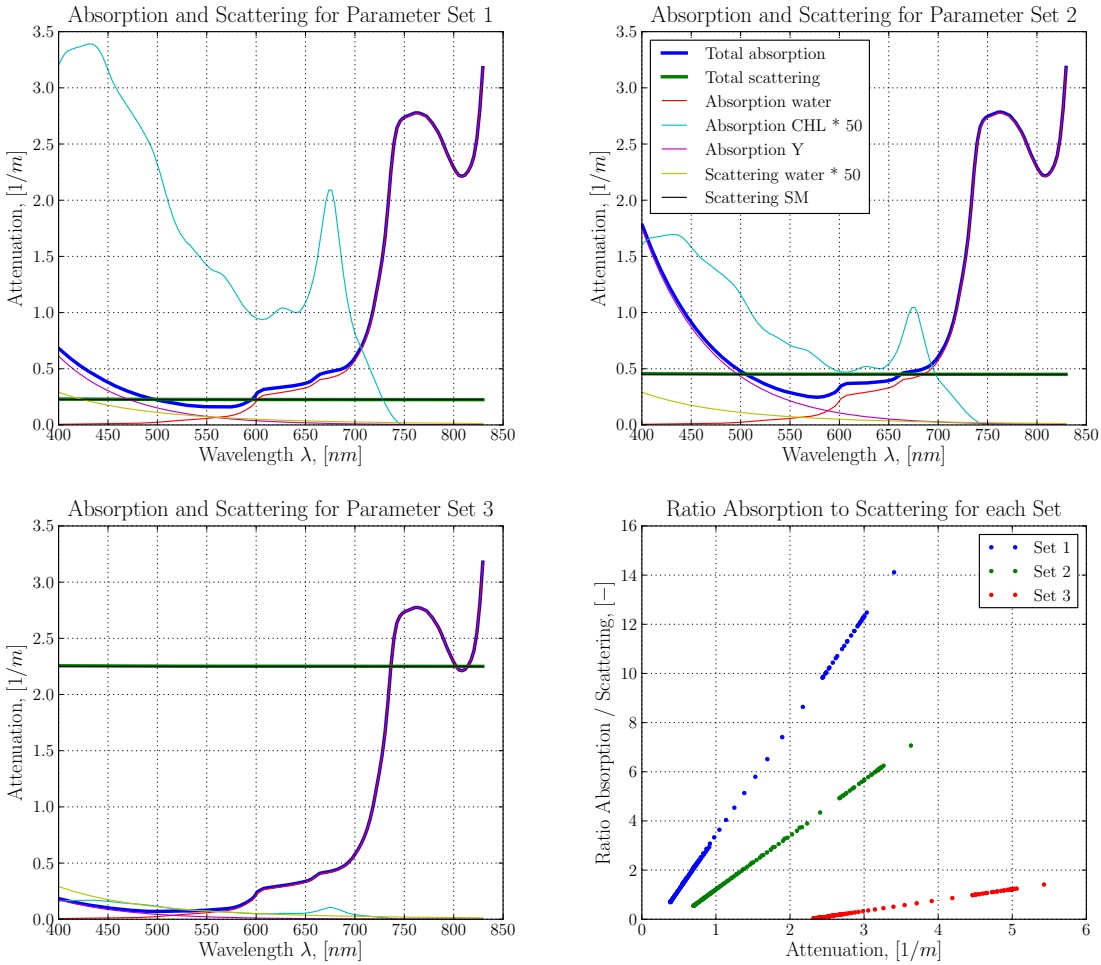

Figure 4.1: Absorption and scattering for all parameter sets (clockwise: set 1, set 2, ratio absorption to scattering, set 3)

- Average horizontal visibility: 39.1 km (turbidity $\beta = 0.1$)
- Humidity: 60%
- Precipitable water content: 1.5 cm
- Ozone: 300 Dobson Units
- Airmass type: 1
- Day of the year: 200
- Solar spectrum: imported from WASI [5]
- Angular distribution of diffuse irradiance: Harrison and Coombes normalized radiances (hcnrad)

The mathematical definition of K_d (equation (2.8)) contains the infinitesimal depth interval $\mathrm{d}z$. In order to calculate K_dd and K_ds numerically a finite depth interval $\mathrm{d}z$ has to be defined over which the attenuation is evaluated. To estimate the effect of this approximation K_dd and K_ds were calculated for five different $\mathrm{d}z$ (0.001 m, 0.01 m, 0.1 m, 0. 5m, 0.99 m) and the relative standard deviation (RSD) over these five curves was calculated. Each calculation was carried out up to a depth of 15 m and was then averaged over all depths. The highest RSD values between the different calculations are 1.39% and 1.34% for the direct and diffuse component with a mean RSD of 0.15% and 0.11% respectively. Hence, K_dd and K_ds are not strongly dependend on the choice of $\mathrm{d}z$ for the calculated unstratified water body. For all further calculations $\mathrm{d}z = 0.01$ m is used.

4.4 Data Processing

In order to process a large varietey of input parameters a workflow was developed to run Hydro-/Ecolight in a semi-automatic batch mode. The three components of the workflow are:

- Creation of batchfile sets, with the desired quantity varied (e.g. sun zenith angle)
- Automated runs of Hydro-/Ecolight with the calculated batchfiles
- Import of the calculated datasets into Python for further analysis

Batchfile Creation

The standard way to operate Hydro-/Ecolight is to use the provided graphical user interface, which creates runfiles containing the desired parameters. This is the best approach if a distinct set of parameters is to be simulated. However, for this work the individual parameters had to be varied in a wide range. Therefore a method to automatically create batchfiles for a given range of parameters was developed. A reference batchfile, with the parameters given in section 4.3, can be modified within an object from this class. The following changes are possible:

- Mission name
- Wavelength range (first wavelength, last wavelength, step size)
- Depths (maximum depth, step size, $\mathrm{d}z$)
- Concentrations (chlorophyll, yellow substance, suspended matter)

- Sky parameters (sun zenith, sun azimuth, cloud cover)
- Component to be calculated (direct, diffuse, both)

Automated Run of Hydrolight

After setting the desired parameters, the new batchfiles can be written either individually or as pairs of direct and diffuse components. A runlist, the list that tells Hydro-/Ecolight which batchfiles to evaluate, for the batchfile set can be created automatically. With the batchfiles and the associated runlist created, Hydro-/Ecolight can be started.

Processing Hydrolight Output in Python: The 'hydrolight' Class

After a successful run of Hydro-/Ecolight the datasets created can be accessed in different ways. The author of the program, Curtis Mobley, developed export routines for Mathworks Matlab, Microsoft Excel and others, but not for Python. In this study, all the data evaluation is carried out in Python and therefore an import routine, to extract the desired quantities from the Hydro-/Ecolight-specific datafiles into Python was developed. The Python class is called 'hydrolight' and offers the following functionality:

- Import
- Extraction of desired quantities into NumPy-arrays
- Plotting of the extracted quantities

4.5 Problems

As mentioned above, Hydrolight divides the hemisphere into 'quads': patches of $10° \times 15°$, per default. All quantities are calculated just for one average solid angle $\Omega(\phi, \theta)$ per quad. An angular resolution of $10° \times 15°$ seems to be a good compromise for most Hydrolight users as the computational time increases quadratically with the amount of quads. Ecolight ignores the ϕ dependecy and calculates only for varying θ angles with a quad (or now rather 'slice') resolution of 10°. The effect of the quad averaging on E_d, E_dd and E_ds is shown in figure 4.2. For the 10° resolution, the irradiances of E_dd and therefore also E_d are discontinuous at the edges of every quad. The diffuse irradiance E_ds doesn't show this behavior. This is most likely due to the fact that the angular light field distribution for the diffuse component in the atmosphere is less peaked than for the direct radiation. The low default angular resolution

leads to inaccurate results for the parameterization of E_{dd}. For that reason the quad size for the calculations in this study was changed to 2°. This leads to much better results as shown in figure 4.2, right side. The computational time is increased by a factor of 25.

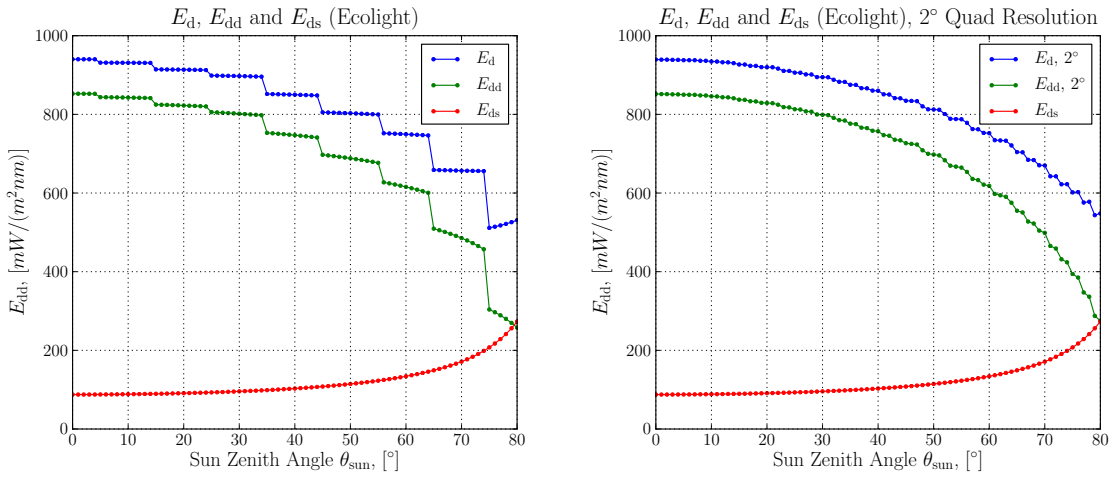

Figure 4.2: Effect of quad averaging on diffuse and direct irradiance computed by Ecolight with 10° (left) and 2° (right) quad resolution at $\lambda = 601.5\,\mathrm{nm}$, $z = 2.0\,\mathrm{m}$.

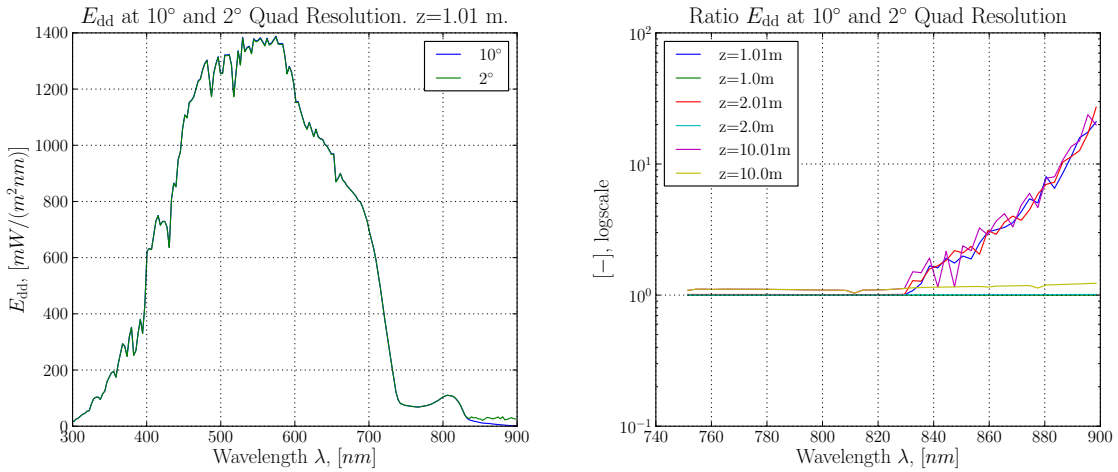

Figure 4.3: Differences at high wavelengths: E_{dd} calculated with 10° and 2° quad resolution at sun zenith angle 0° and parameter set 1 (section 4.3).

Surprisingly, a 2° quad resolution leads to quite different results in irradiances for values at wavelengths above approximately 730 nm . This numerical problem also seems to be sensitive on the geometrical depth: for depth values like 1.00, 2.00, 3.00, ... m the difference is orders of magnitude smaller than for values like 1.01, 2.01, 3.01, ... m (which are needed for the calculation of K_{d} with $\mathrm{d}z = 0.01\,\mathrm{m}$). In figure 4.3 an example for this problem is given. The reason for this behavior is not completely understood, but according to the author of Hydro-/Ecolight, it could be due to numerical problems with solving the RTE for very low

intensities. In the problematic wavelength regions, pure water absorbs highly and therefore only little intensity is left at bigger depths. This is the reason why field measurements, as well as numeric simulations, are problematic at those wavelengths. The same argumentation is valid for wavelengths below 400 nm, due to absorption of yellow substance instead of water (figure 4.1). The calculations of the diffuse component are less affected by this problem, most likely because the 10° angular resolution performs numerically more efficient. As a consequence of those numeric limitations, only a wavelength range of 400 - 730 nm and 400 - 830 nm could be used for the simulations of the direct and diffuse components, respectively.

A rather minor problem with Hydro-/Ecolight occurs at very low calculated intensities. When a value falls below $1 \cdot 10^{-99}$, which is denoted in the output files as '1E-99', Hydro-/Ecolight skips the 'E' and writes '1-100' instead of '1E-100'. As such an expression is a valid mathematical statement, it is interpreted by the Python routines as '$1 - 100 = 99$', which leads to high peaks in the plotted spectra. A subroutine checks for the occurence of this bug and corrects, if necessary.

5 Measurements and Data Analysis

In this chapter the field measurements of under water downwelling irradiances are explained. This includes a description of the measurement purpose, the location and conditions, the instrument and the setup. The measurement procedure and the data handling are covered in the second part, followed by a short introduction of WASI, the software which is the interface between the measurements and the analytical model to be validated.

5.1 Measurement Purpose and Conditions

Numeric simulations with Hydro-/Ecolight are not able to simulate the influences of the wave-focusing effect on the changes in intensity of the direct and diffuse downwelling irradiance components. The numeric code is capable of simulating wave-slope statistics of wind-blown water surfaces. This does affect the under water light field distribution but does not simulate the intensity variabilities induced by the wave-focusing effect. For this reason, field measurements were necessary to validate the analytical description of downwelling irradiance in water, as described in chapter 3. The model extrapolates the incident irradiance just below the water surface to larger depths, as stated in equation (3.2). As the newly developed parameterizations for $\overline{K}_{\mathrm{dd}}$ and $\overline{K}_{\mathrm{ds}}$ are part of the analytical description, an independent validation can be achieved also for those. To validate the model, the downwelling irradiance in different depths was measured. In a second step, the measured spectra were used to fit the analytical model. The sensor depth retrieved through the fits is compared with independent measurements. As the model accounts for the wave-focusing effect, the variability of the fitted sensor depths should be significantly lower than for conventional models, such as the model of Gordon (equation (2.19)). As the field measurements were not carried out to depths higher than about three meters, only a qualitative validation of the $\overline{K}_{\mathrm{dd}}$ and $\overline{K}_{\mathrm{ds}}$ parameterizations is expected from the fit results. To be sure that the model performs well in various situations, measurements under different conditions were carried out. Datasets in different constellations of the following parameters were collected for this study:

- Depth
- Cloud cover

- Sun zenith angle
- Water surface roughness
- Bottom albedo

The measurements took place at Lake Starnberg, which is located south of Munich, Germany. With an area of about 60 km^2 and a north-south extent of more than 20 km it is the fifth biggest lake in Germany. The measurements were taken at two sites, a jetty in Starnberg (N 47.9963°, E 11.3495°) at the northern shore and a jetty in Seeshaupt (N 47.8214°, E 11.3208°) at the southern shore.

The data of the following field trips entered the final verification process:

Table 5.1: Details of measurements at location 'Mole Starnberg' and 'Lido Seeshaupt'

Acronym	M1	M2	M3	L1	L2
Date, [dd-mm-yy]	11-10-10	16-06-11	28-06-11	04-10-10	17-05-11
Time, [hh:mm]	14:15-15:45	14:00-15:30	19:45-21:15	15:30-16:30	11:30-13:30
Max. depth, [cm]	277	243	193	131	117
Depth step size, [cm]	30	30	30	30	50
Measurements, [#]	360	276	329	230	251
Cloud cover, [%]	0	100	0	0	100
Sun zenith angle, [°]	57-65	27-37	78-90	61-68	29-34
Wave height, [cm]	5	3	3	5	10
Bottom type	macroph.	sediment	macroph.	macroph.	sediment

5.2 Instrument

The spectral measurements of the downwelling irradiances were carried out with a RAMSES ACC-VIS hyper-spectral radiometer (hereafter: RAMSES) manufactured by *TriOS Mess- und Datentechnik GmbH* (Oldenburg, Germany, hereafter: Trios). The instrument is based on a 'MMS1' spectrometer, manufactured by *Carl Zeiss MicroImaging GmbH* (Jena, Germany) and is specified by Trios on a wavelength range of 320-950 nm with an average spectral resolution of 3.3 nm and a spectral accuracy better than 0.3 nm [16].
RAMSES is equipped with a cosine collector built of synthetic fused silica with a deviation from a perfect cosine response of less than 2 % for zenith angles less than 70° and less than 3.5 % for zenith angles between 70° and 90°. From the cosine collector the light is transmitted by an optical fiber to a holographic grating, where it gets spectrally dispersed and then detected by a photo diode array (256 channels). Of those channels, 19 are used for dark current correction.

Figure 5.1: Trios RAMSES ACC VIS assembled (left) and with housing removed (right) [1]

The spectral calibration of the instrument was carried out once by the sensor manufacturer before delivery. The radiometric calibration was done by Trios with a NIST-traceable FEL lamp (DXW-1000W, 120V) which is calibrated by a subcontractor called *Gigahertz-Optik GmbH* (Türkenfeld, Germany) according to NIST standards.

Because the radiometric calibration of the used irradiance sensor (RAMSES ACC-VIS, serial number: 806f) was carried out more than two years before the field measurements, the calibration was validated with a NIST-traceable FEL lamp (GAMMA SCIENTIFIC 5000-16C, serial number: GS1033, calibrated 16. Oct 2009). The result was a mean deviation over all wavelength of 8.1 % with a maximal deviation of over 14 % for wavelengths next to 350 nm. In the range of wavelengths used for this study of 400 - 830 nm, the wavelength error was negligible. As for the fit of sensor depths with WASI (section 5.6), the absolute intensities are not from great importance, the calibration by Trios was used for the data evaluation.

5.3 Measurement Setup

The RAMSES sensor is connected to a controller box which can deal with up to four RAMSES sensors at the same time. The controller box is connected via a RS232 cable to a notebook which triggers the measurements and collects the data with a software called MSDA_XE, which is provided by Trios.

For this study, only the downwelling irradiance E_d is from interest, but for further use of the collected dataset also the upwelling irradiance E_u and the upwelling radiance L_u are measured with two more RAMSES sensors: The E_u sensor (RAMSES ACC-VIS, serial number: 8050) is identical in construction to the E_d-sensor, the L_u-sensor (RAMSES ARC-VIS SN, serial number: 808f) measures radiance with a field of view of 7° in air [1]. Additionally the

downwelling irradiance above the surface $E_d(z = 0^+)$ was measured occasionally with a fourth RAMSES ACC sensor (RAMSES ACC-VIS, serial number: 8109) to check whether the illumination conditions remained stable during the measurements (lower right picture in figure 5.2). One of the used sensors (RAMSES ACC-VIS, serial number: 808f) was equipped with inclination and pressure sensors. The inclination is measured for angles less than 45° along two perpendicular axes, each parallel to the cosine collector with an accuracy better than 1°. The pressure sensor is specified from 0 to 10 bar with an accuracy better than 0.025 bar. However, those data were not used within this study.

The measurements were carried out from jetties with the setup in figure 5.2, consisting of a cantilever arm build onto a movable construction. The sensors are hold in place by a mount which is attached to two wire ropes and can be submersed to 8 m below the water surface. The mount itself is balanced out in the water, so that the sensors are aligned normally to the water surface. The up- and downwards measuring sensors are aligned in one horizontal plane relative to their entry optics. A measuring tape connects the cantilever arm with the sensor mount to have reliable, independent readings of the actual sensor depth.

The two measurement sites are the jetties of the *Bayerische Seen-Schifffahrt* in Starnberg and of the *Seerestaurant Lido* in Seeshaupt, as described in section 5.1. Both offer a stable platform and remoteness from possibly shading constructions. The cantilever arm has a length of 5 m, so that shading by the jetties is minimized. However, the maximal depth measurable from those jetties is limited to about three meters, depending on the water-level of Lake Starnberg.

5.4 Measurement Procedure

The irradiance depth profile measurement starts with the sensors above the water surface to measure the incident radiation ($E_d(0^+)$) followed by the measurement just below the surface ($E_d(0^-)$). Consequently, measurements in fixed depth intervals are taken (usually 0.3 or 0.5 m) until the sensor mount touches the ground. The last measurement is another take of $E_d(0^+)$ to check if the illumination conditions remained stable during the acquisition (which can be skipped for campaigns with a fourth E_d sensor above the surface). Every measurement consists of several takes (usually 30) to have an estimation of the variability in the signal. The integration time is automatically set by MSDA_XE for each sensor individually (4 ms - 8 s). The data takes are triggered simultaneously. However, as the up- and down looking sensors receive very different intensities, the integration times differ. Therefore the measurements are not strictly simultaneous. The repetition rate is mainly limited by the RS232 interface. With four sensors connected to the controller box the minimal repetition rate is about 15 seconds. A typical measurement thus takes about 8 min.

Figure 5.2: Measurement setup: measurement construction (top left), sensor mount (top right), sensor mount partially submersed (lower left), above water downwelling irradiance sensor (lower right).

The sensor depth is read from the measuring tape. The readings are taken directly at the water surface to have an estimation of the error in the depth readings, at least at the time of the reading, as wave conditions can vary quite a lot during one measurement of 8 min. Currents turned out to be problematic as they can slowly bulge the tape during a set of measurements.

5.5 Data Handling

The final product of the data analysis is a value of the sensor depth for each measurement. This value is determined by the public domain software WASI [5] by fitting the developed analytical model (chapter 3) to the measured under water spectra. The model used for the calculation of the downwelling irradiance just above the water surface is the analytic model of Gregg and Carder [9]. It assumes a cloudless, maritime standard atmosphere.

In order to fit the acquired data with WASI, it is necessary to convert them to a WASI readable data format and to add some additional information to it. As a first step, the measurements need to be exported from the MSDA_XE database. Because each sensor has

slightly different central wavelengths, a resampling to a common wavelength grid is performed before exporting the data to ASCII files. Then a set of Python scripts sorts the files into a directory structure, according to sensor name and measurement identification tag. In this process also two calculated parameters are added to the files: the sun zenith angle of each measurement and the according day of the year. As a last step, the data is converted to a WASI readable format.

5.6 WASI Fits

WASI can be run in batch mode to automatically fit a set of measurements. To achieve an optimal fit of the sensor depth, the atmospheric parameters in the used Gregg and Carder model have to be fitted to the the above water spectra. Those parameters are: ozone scale height H_{oz}, Angström exponent α, turbidity coefficient β and water vapor concentration WV. For the measurements with an additional $E_{\mathrm{d}}(0^+)$ sensor, the mean value for these parameters over the whole set of measurements is taken, otherwise the mean values of the measurement at $z = 0^+$. The determined values are set constant for the subsequent under water fits. Those are performed with the following parameters and start values:

- phytoplankton concentration $C[4] = 2.0$ mg m^{-3}
- large particles concentration $C_{\mathrm{L}} = 0.6$ g m^{-3}
- yellow substance concentration $C_{\mathrm{Y}} = 0.3$ m^{-1}
- yellow substance exponent $S = 0.016$ nm^{-1}
- depth $z = 2.0$ m
- fraction of direct radiation f_{dd}[1] $= 1.0$
- fraction of diffuse radiation $f_{\mathrm{ds}} = 1.0$

The correct sun zenith angle for each measurement is calculated automatically, as mentioned above. The values for the Q-factor and the water temperature are set to Q = 0.5 and $\mathrm{T_w} = 20.0\,^{\circ}\mathrm{C}$. The fits are performed in a wavelength range of 400 to 800 nm and a data interval of 3 nm. The quantity minimized during the fit procedure was set to least squares. The fit of the sensor depth is slightly dependent on the yellow substance exponent S. As independent measurements of S were not performed within this study, S had to be included as a fit parameter. The results of the fits for all parameters are written in an ASCII file which is read in by a Python script for further evaluation. In figure 5.3, the graphical user

[1] as explained in chapter 3

interface of WASI is shown, with an exemplary spectrum and its corresponding model fit. The peaked shape of the fit curve in comparison to the measurement spectrum is due to the higher spectral resolution of the input spectra used by WASI.

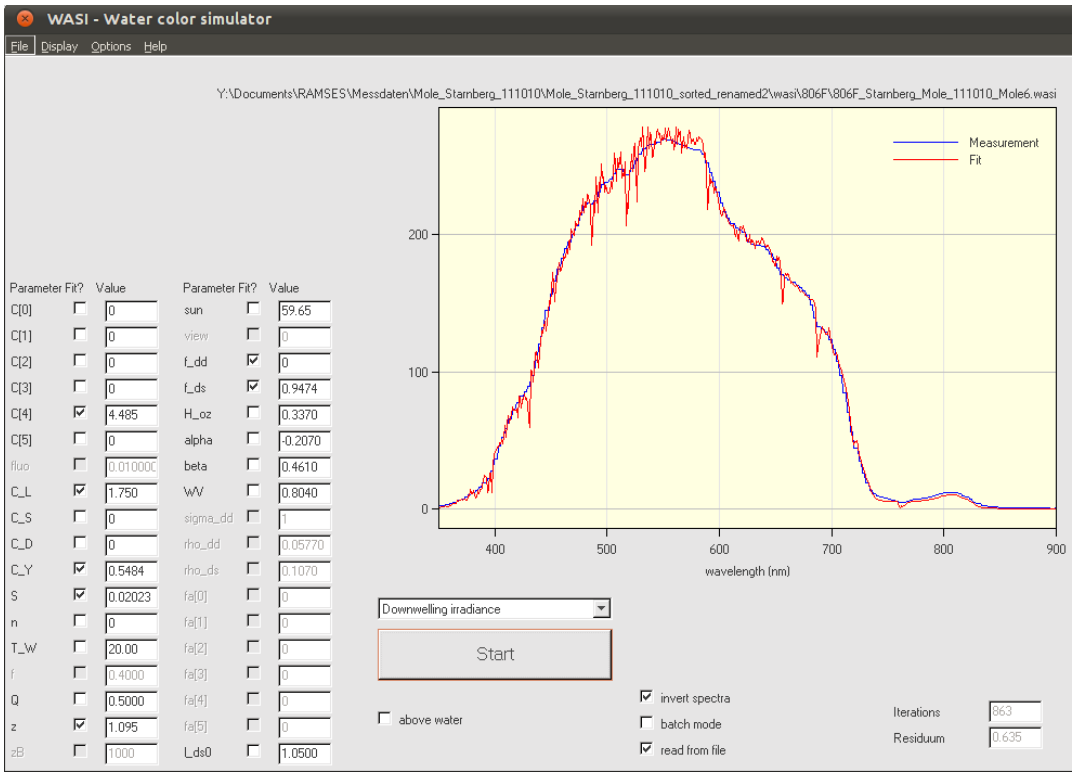

Figure 5.3: WASI - Water color simulator by Peter Gege. Measurement of downwelling irradiance and corresponding fit curve.

6 Results

The results are presentend in four sections: first the numerical simulations of $\overline{K}_{\mathrm{dd}}$ and $\overline{K}_{\mathrm{ds}}$ are shown. The simulations were the basis for the development of a parameterization which is shown secondly. The result of the comparisons between the new models and different reference models are treated in the third section. As an independent verification of the new irradiance model, including a $\overline{K}_{\mathrm{dd}}$ and $\overline{K}_{\mathrm{ds}}$ parameterization, the inversion of the sensor depth from field measurements is shown in the last part.

6.1 Simulations of $\overline{K}_{\mathrm{dd}}$ and $\overline{K}_{\mathrm{ds}}$

In order to find a good parameterization for $\overline{K}_{\mathrm{dd}}$ and $\overline{K}_{\mathrm{ds}}$, it was necessary to simulate the quantities separately. This was done with a modified Ecolight version, as described in section 4.2. The simulations for $\overline{K}_{\mathrm{dd}}$ were carried out with Ecolight, modified to work with 2° quad resolution, as described in section 4.5. The wavelength range was limited to 400 - 730 nm for the $\overline{K}_{\mathrm{dd}}$ simulations and 400 - 830 nm for the $\overline{K}_{\mathrm{ds}}$ simulations to avoid numerically and experimentally problematic high attenuation values, also as described in section 4.5. All simulations were performed for the three parameter sets defined in section 4.3. For brevity, the figures in this section only show the results for parameter set 1, which represents the measurement conditions in this study.

The approximation of K_{d} as $(a + b_{\mathrm{b}})/\cos\theta^{\mathrm{w}}_{\mathrm{sun}}$ is a reasonable first step to a parameterization of K_{d}, as explained in chapter 2. The question to be answered is if this assumption also hold for the separated coefficients $\overline{K}_{\mathrm{dd}}$ and $\overline{K}_{\mathrm{ds}}$. In figures 6.1 and 6.2, $\overline{K}_{\mathrm{dd}}$ and $\overline{K}_{\mathrm{ds}}$ are plotted for a sun zenith angle of 0° and 80° and for depths just below the surface to 10 m. Each attenuation coefficient is plotted in two different ways: as a function of wavelength and of $(a + b_{\mathrm{b}})/\cos\theta^{\mathrm{w}}_{\mathrm{sun}}$ or $(a + b_{\mathrm{b}})$ (for $\overline{K}_{\mathrm{dd}}$ and $\overline{K}_{\mathrm{ds}}$, respectively), to show the validity of those approximations for different depths and sun zenith angles.

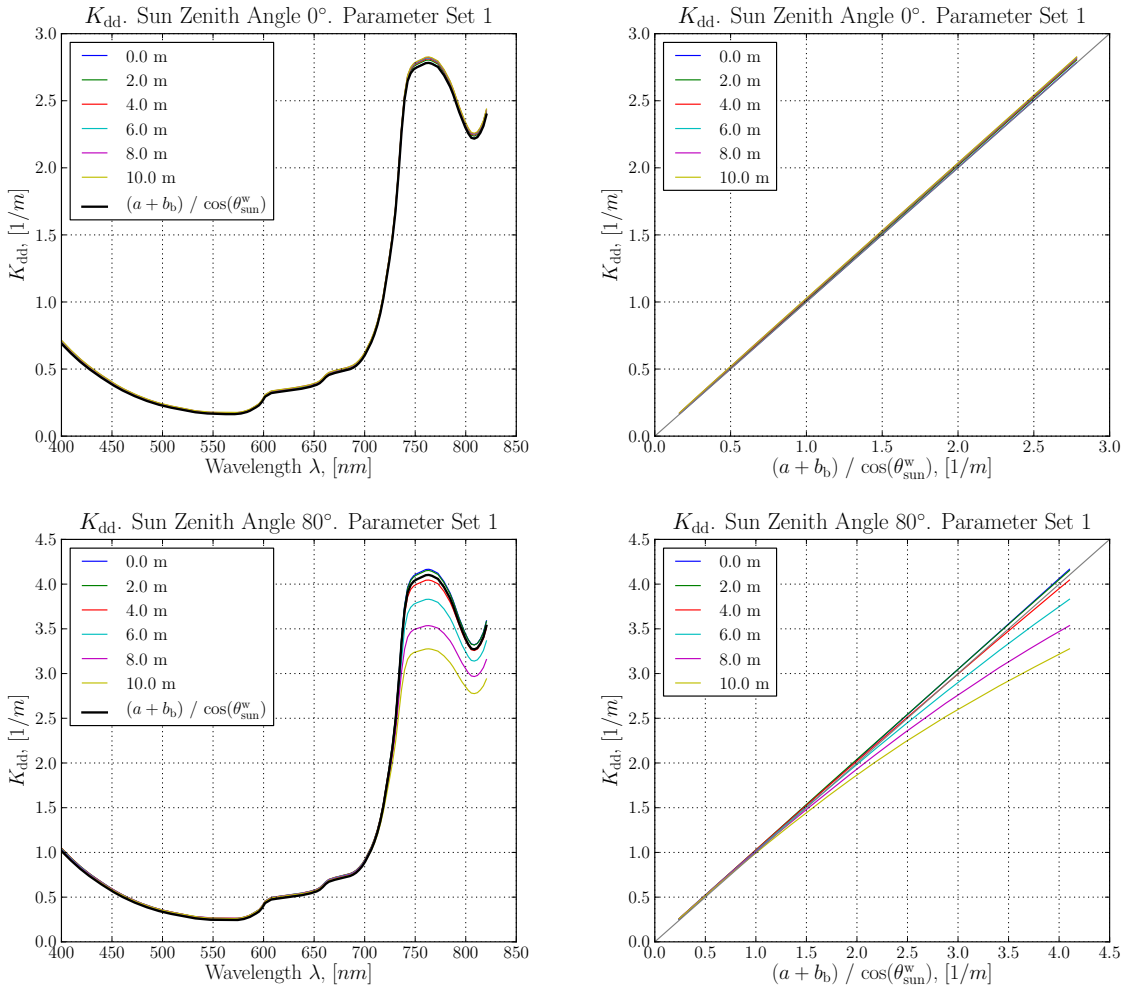

Figure 6.1: $\overline{K}_{dd}$ at sun zenith 0° and 80° (upper, lower panel). Left side: plotted against wavelength. Right side: plotted against $(a + b_b)/\cos(\theta^w_{sun})$. Calculated with parameter set 1, section 4.3.

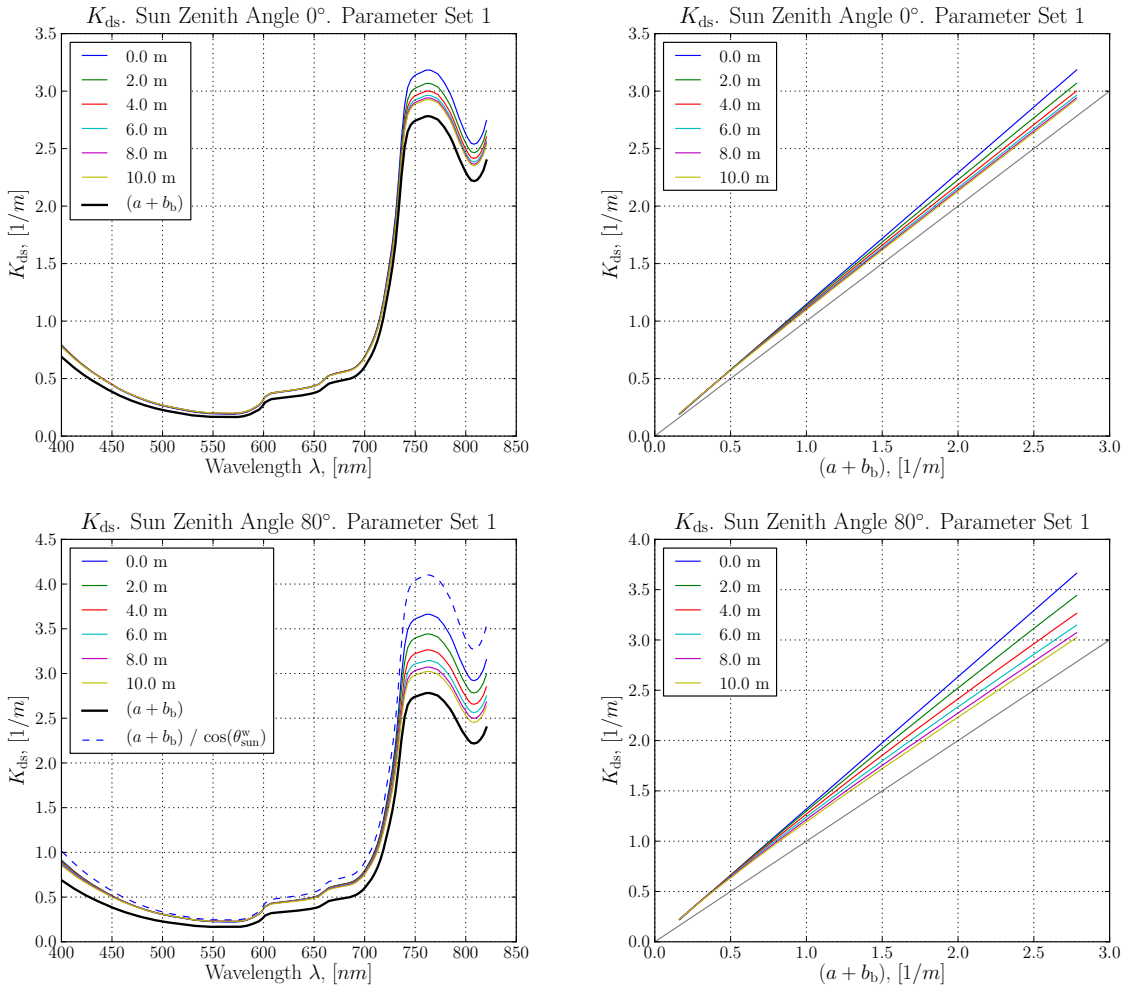

Figure 6.2: $\overline{K}_{\mathrm{ds}}$ at sun zenith 0° and 80° (upper, lower panel). Left side: plotted against wavelength. Right side: plotted against $(a + b_{\mathrm{b}})$. Calculated with parameter set 1, section 4.3.

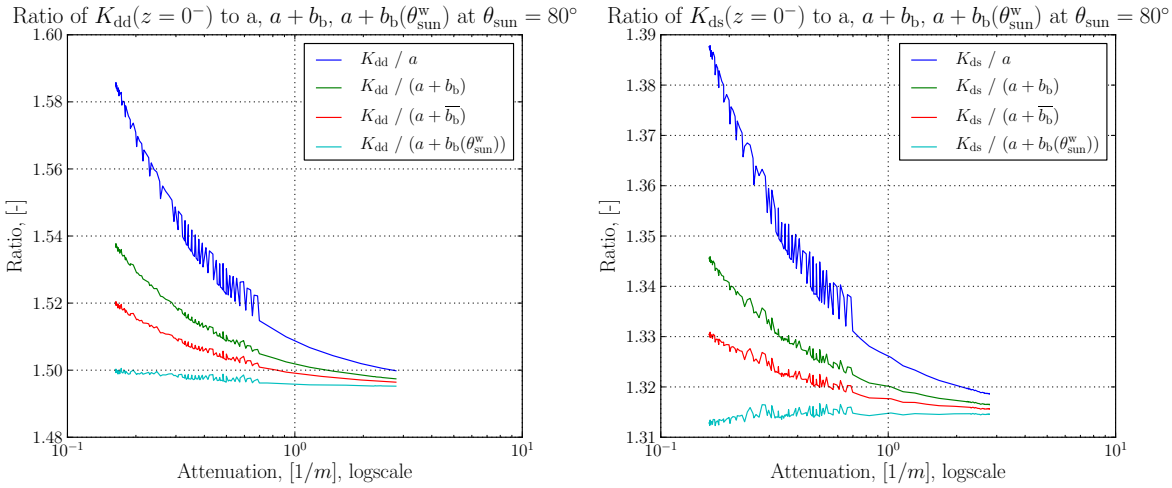

Figure 6.3: Ratio of $\overline{K}_{dd}$ (left) and $\overline{K}_{ds}$ (right) to different approximations: a, $a+b_b$, $a+\overline{b_b}$ and $a+b_b(\theta^w_{sun})$. Sun zenith angle: 80°. Calculated with parameter set 1, section 4.3.

6.2 New Parameterization of $\overline{K}_{dd}$ and $\overline{K}_{ds}$

With the simulations of K_{dd} and K_{ds} for different water constituent concentrations, a parameterization was developed for the mean K_{dd} and K_{ds} over the euphotic zone. The 10 % and 1 % levels[1] were determined separately for each wavelength. To find a water constituent independent solution was a main priority as most existing parameterizations are limited to absorption dominated water bodies. Due to the sun zenith angle dependent backscattering coefficient, a good result also for high sun zenith angles is expected. To emphasize the possibilities created by the modifications on Hydro-/Ecolight, the diffuse component of the Pan-Zimmerman model was improved and included in the comparison.

6.2.1 Sun Zenith Angle dependent Backscattering Coefficient

As explained in section 2.2.4, it is possible to improve the approximation of b_b (which is only valid for the sun at zenith position) by calculating a sun zenith angle dependent backscattering coefficient $b_b(\lambda, \theta^w_{sun})$, using equation 2.15. The effect of this calculation is shown in figure 6.3. In the plots a high sun zenith angle of 80° is used, to pronounce the effect of the correction. In the parameterizations below, $\overline{b_b}(\lambda)$ denotes the average $b_b(\lambda, \theta^w_{sun})$ over all sun zenith angles (from 0° to 90°), as defined in equation 2.17.

[1] The 10 % or 1 % level is the depth, where only 10 % or 1 % of the intensitiy just below the surface is left. This depth is dependent on wavelength. The euphotic zone of the water column ranges from the surface to the 10 % or 1 % level, depending on definition.

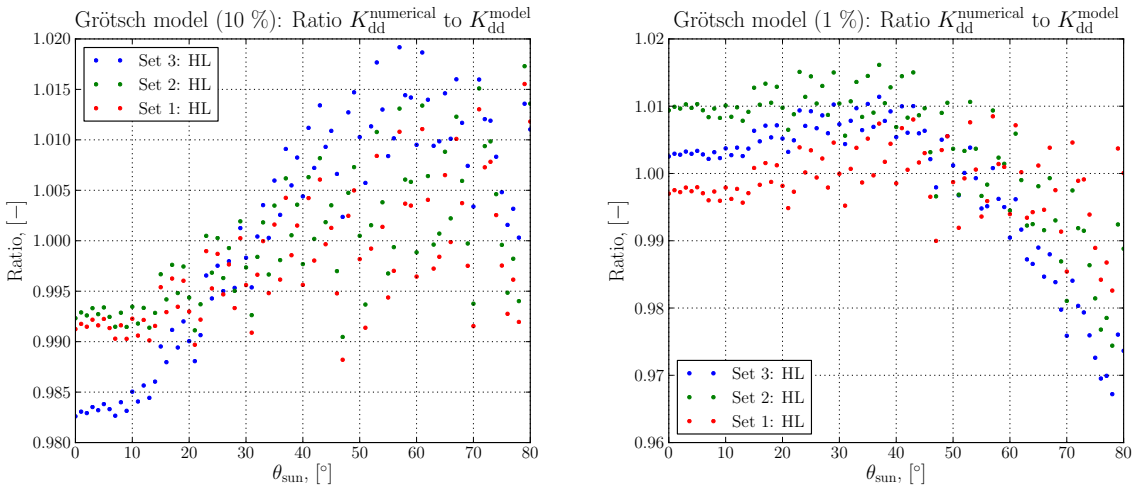

Figure 6.4: Ratio of numerical and modeled $\overline{K}_{\mathrm{dd}}$ (equation (6.1)). K_{dd} values were averaged down to the 10 % (left) and 1 % (right) depth level and over all wavelengths. Calculations were performed for each set of section 4.3.

6.2.2 Parameterization of $\overline{K}_{\mathrm{dd}}$

The simulated $\overline{K}_{\mathrm{dd}}$, averaged down to the 10 % and 1 % level, were used to find a parameterization which performs well for all calculated parameter sets, as listed in section 4.3. The developed parameterization of $\overline{K}_{\mathrm{dd}}$,

$$\overline{K}_{\mathrm{dd}}(\lambda, \theta_{\mathrm{sun}}^{\mathrm{w}}) \quad = \quad l_{\mathrm{a}} \cdot \frac{a(\lambda)}{\cos\theta'_{sun}} + l_{\mathrm{b}} \cdot \overline{b_{\mathrm{b}}}(\lambda) \tag{6.1}$$

is valid with parameters $l_{\mathrm{a}} = 1.017$ and $l_{\mathrm{b}} = 1.95$ or $l_{\mathrm{b}} = 2.04$ for $\overline{K}_{\mathrm{dd}}$ averaged to the 10 % or 1 % depth level, respectively. The parameterization can be used for absorption and scattering dominated waters. In figure 6.4 the performance of this parameterization for the different water constituent concentration sets is plotted. The mean ratio over all sun zenith angles, wavelengths, depths and parameter sets is 0.9997 ± 0.0085 and 1.0004 ± 0.0096 (10 % and 1 % depth level, respectively). The largest absolute deviations are 1.92 % and 3.28 %, respectively.

6.2.3 Parameterization of $\overline{K}_{\mathrm{ds}}$

For the parameterization of $\overline{K}_{\mathrm{ds}}$, two models were developed. Both use the same sun zenith angle parameterization:

$$l_{\theta}(\theta_{\mathrm{sun}}^{\mathrm{w}}, m, n) \quad = \quad m + n \cdot (1 - \cos\theta_{\mathrm{sun}}^{\mathrm{w}}). \tag{6.2}$$

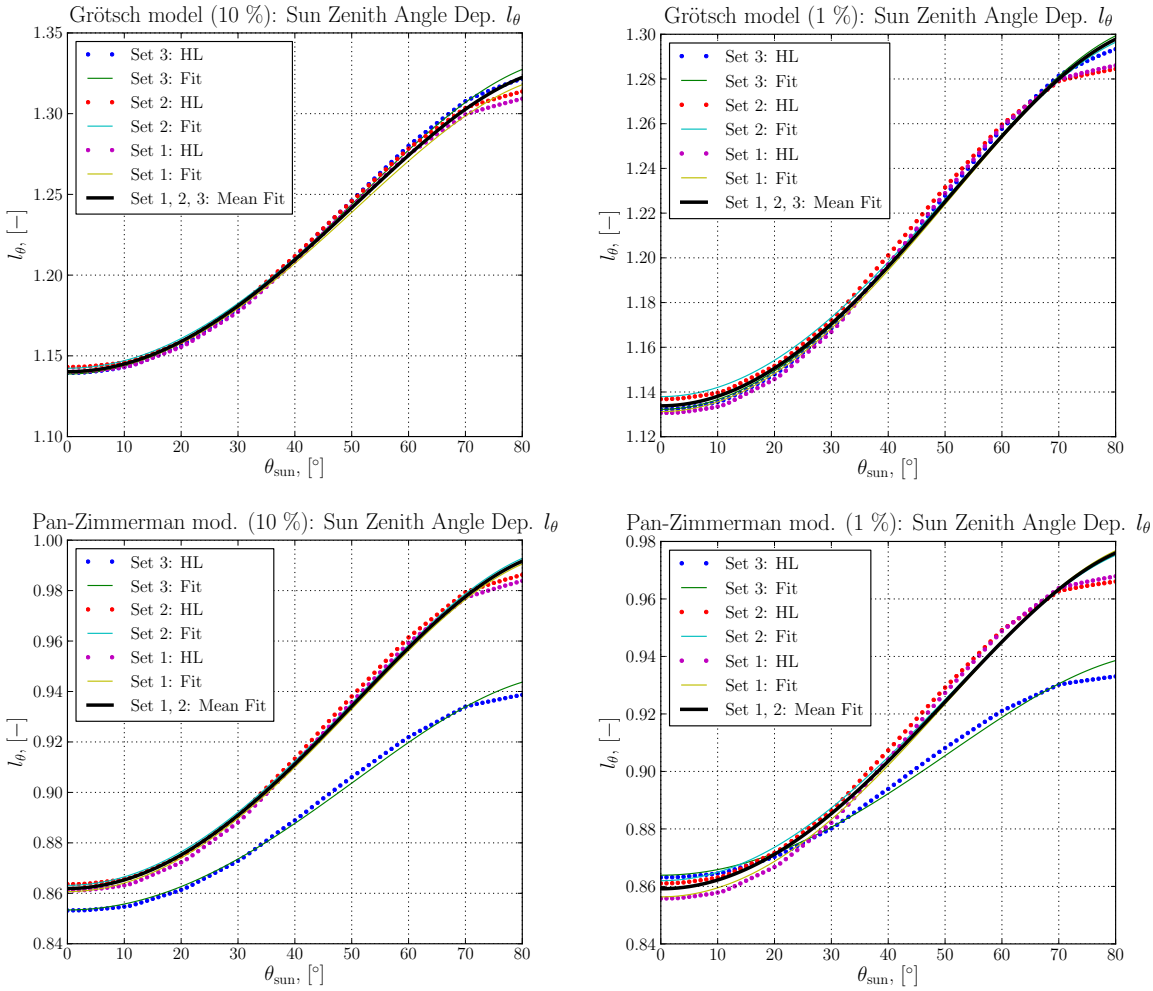

Figure 6.5: Fit of sun zenith angle parameterization $l_\theta(\theta^{\text{w}}_{\text{sun}}, m, n)$ for the Grötsch and modified Pan-Zimmerman model. K_{ds} values were averaged to the 10 % (left) and 1 % (right) depth levels and over all wavelengths. Calculations were performed for each parameter set of section 4.3.

For the determination of the parameters m and n, the numerical values for $\overline{K}_{\text{ds}}$ (depth-averaged from the surface to the 10 % and 1 % intensity levels) are averaged over all used wavelengths. The model parameterizations (equations 6.3 and 6.4), with l_θ set to one, are plotted against those averages. The resulting curve is used as the input for the fit of l_θ. This is done for both models and each parameter set. The results are plotted in figure 6.5. For the Grötsch model, the fits for all parameter sets are similar in shape. The average over all three fit curves is used for the final parameterization. As the modified Pan-Zimmerman model was not independent of the water constituent concentrations, separate pairs of parameters m, n had to be calculated for the absorption dominated sets 1 and 2 and the scattering dominated set 3.

Grötsch Model

The sun zenith angle dependency is covered by $l_\theta(\theta^{\mathrm{w}}_{\mathrm{sun}}, m, n)$. To achieve a water constituent independent solution, an additional term was necessary to cover the effects of multiple scattering. This term scales with the cosine of the under water sun zenith angle and therefore yields the highest corrections for the sun at zenith position. The developed parameterization of $\overline{K}_{\mathrm{ds}}$,

$$\overline{K}_{\mathrm{ds}}(\lambda, \theta^{\mathrm{w}}_{\mathrm{sun}}) = \left[a(\lambda) + \overline{b_{\mathrm{b}}}(\lambda) + l_{\mathrm{ms}} \cdot \overline{b_{\mathrm{b}}}(\lambda) \cdot \cos(\theta^{\mathrm{w}}_{\mathrm{sun}})\right] \cdot l_\theta(\theta^{\mathrm{w}}_{\mathrm{sun}}, m, n), \tag{6.3}$$

is valid with parameters $m = 1.140$, $n = 0.556$, $l_{\mathrm{ms}} = 1.128$ or $m = 1.133$, $n = 0.500$, $l_{\mathrm{ms}} = 1.312$ for $\overline{K}_{\mathrm{ds}}$ averaged to the 10 % or 1% depth level, respectively. The parameterization can be used for absorption and scattering dominated water bodies. The performance of this parameterization in comparison to the numerical solution is plotted in figure 6.6 for each water constituent set and for the average to the 10 % and 1 % depth levels. The mean ratios over all wavelengths, depths, sun zenith angles and parameter sets, for the 10 % and 1 % depth levels are 1.0000 ± 0.0020 and 1.0000 ± 0.0027. The largest absolute deviations are 0.32 % and 0.44 %, respectively.

Modified Pan-Zimmerman Model

As mentioned before, the diffuse component of the Pan-Zimmerman model was optimized to Hydrolight calculations with the sun at a sun zenith angle of 89° to simulate a quasi diffuse light field distribution. As the modification of Hydro-/Ecolight creates the possibility to simulate the diffuse light field distinctly for all sun zenith angles, the existing model could be improved. The modification consists of an additional term to account for the sun zenith dependency of the diffuse irradiance. As the original model parameters were calculated for different light field conditions, a water constituent concentration independent parameterization couldn't be found during this study. The modified Pan-Zimmerman model,

$$\begin{aligned}
\overline{K}_{\mathrm{ds}}(\lambda, \theta^{\mathrm{w}}_{\mathrm{sun}}) &= \overline{K}^{\mathrm{PZ}}_{\mathrm{ds}}(\lambda) \cdot l_\theta(\theta^{\mathrm{w}}_{\mathrm{sun}}, m, n) \\
\overline{K}^{\mathrm{PZ}}_{\mathrm{ds}}(\lambda) &= \left(p_0 - A_0\omega_0 - A_1\omega_0^2\right) \cdot c \\
A_0 &= p_1 + p_2(\tilde{b_{\mathrm{b}}})^{0.5} + p_3\tilde{b_{\mathrm{b}}} \\
A_1 &= p_4 + p_5(\tilde{b_{\mathrm{b}}})^{0.5} + p_6\tilde{b_{\mathrm{b}}} \\
\tilde{b_{\mathrm{b}}} &= \frac{b_{\mathrm{b}}}{b} \\
\omega_0 &= \frac{b}{c} \\
c &= a + b
\end{aligned} \tag{6.4}$$

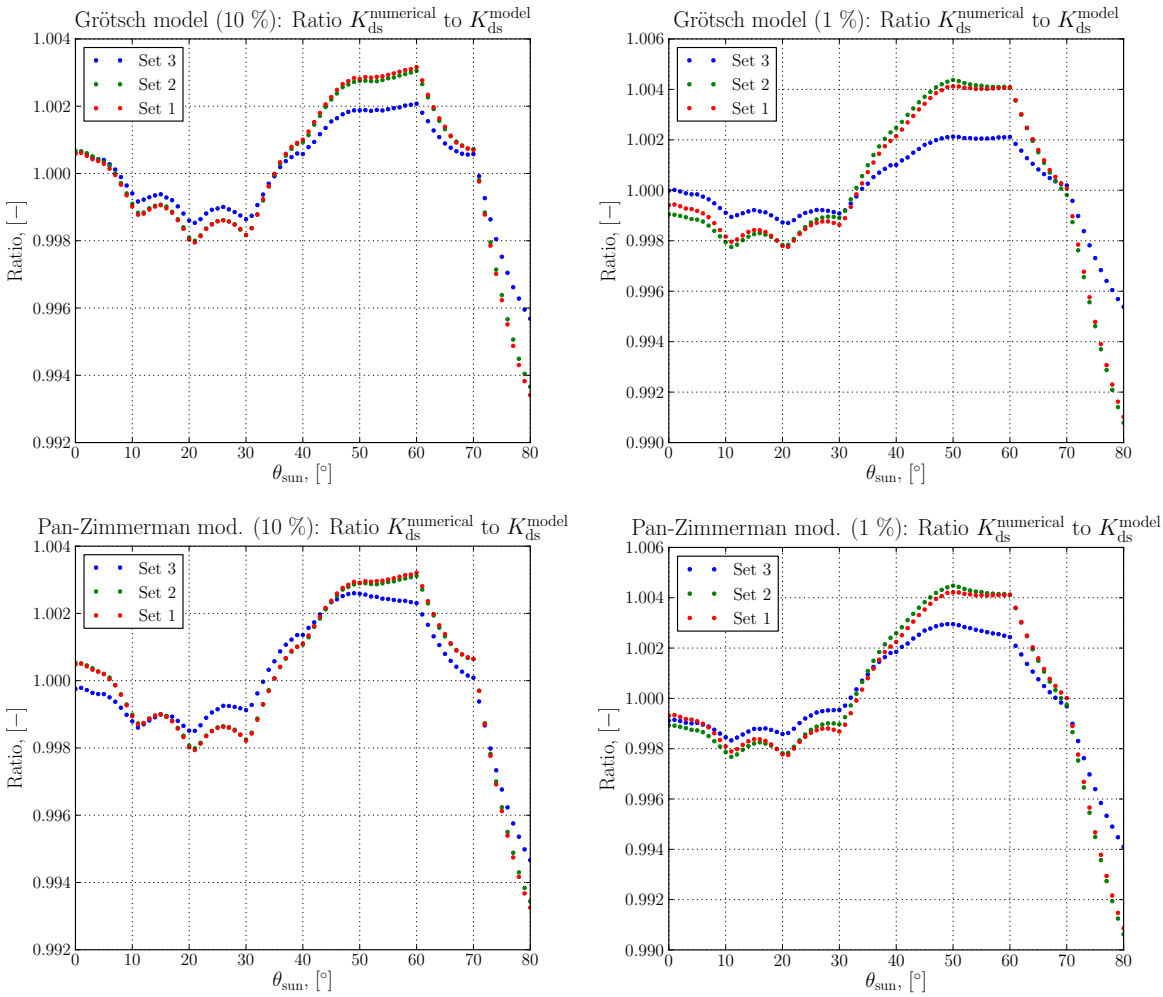

Figure 6.6: Ratio of numerical and modeled $\overline{K}_{ds}$ for the Grötsch (equation (6.3)) and modified Pan-Zimmerman model (equation (6.4)). K_{ds} values were averaged down to the 10 % (left) and 1 % (right) depth level and all wavelengths. Calculations were performed for each set of section 4.3.

with parameters $p_0 = 1.317$, $p_1 = 1.399$, $p_2 = -1.012$, $p_3 = -0.939$, $p_4 = -0.047$, $p_5 = 0.244$, $p_6 = 1.120$, differs from its original version [17] by the factor $l_\theta(\theta_{sun}^w, m, n)$ for the sun zenith dependency. The parameters for l_θ are $m = 0.862$, $n = 0.396$ or $m = 0.859$, $n = 0.356$ for absorption dominated water bodies and the 10 % or 1 % level, respectively. For scattering dominated waters, parameters $m = 0.853$, $n = 0.275$ or $m = 0.864$, $n = 0.228$ are valid for the 10 % or 1 % level, respectively. Also for this model, figure 6.6 shows the ratio of numerically calculated and modeled $\overline{K}_{ds}$. The mean ratios over all wavelengths, dephts, sun zenith angles and parameter sets for the 10 % and 1 % depth levels, are 1.0000 ± 0.0022 and 1.0000 ± 0.0029. The largest absolute deviations are 0.32 % and 0.45 %, respectively.

6.3 Comparison

To quantify the errors resulting from the $\overline{K}_{\mathrm{dd}}$ and $\overline{K}_{\mathrm{ds}}$ models, the downwelling irradiances E_{dd}, E_{ds} and the combined downwelling irradiance $E_{\mathrm{d}} = E_{\mathrm{dd}} + E_{\mathrm{ds}}$ are calculated according to equation 3.2. The relative and absolute deviations of the model results, compared to the numerical solutions, are plotted in figures 6.7, 6.9 and 6.11. For those figures, the deviations are averaged over all used wavelengths and depths and plotted against the sun zenith angle. In figures 6.8, 6.10 and 6.12, the relative deviations are plotted against wavelength and depth (averaged over sun zenith angle and depth or wavelength, respectively). The absolute deviations are just shown for the plots against sun zenith angle, as they are primarily dependent on the mean intensity level. The mean intensity level also changes with sun zenith angle, but usually significantly less than with wavelength or depth. In the Gege-Pinnel model, the backscattering coefficient b_{b} is used. To show the effect of $b_{\mathrm{b}}(\theta^{\mathrm{w}}_{\mathrm{sun}})$, a second Gege-Pinnel model with the sun zenith angle dependent backscattering coefficient is included in the comparison. In the comparison of the E_{d} models, also the Gordon[1975] [8] model is included as a representative K_{d} model. For E_{d}, the direct and diffuse parts of the Pan-Zimmerman and modified Pan-Zimmerman models were used independently instead of the analytical separation of E_{d}, offered by the authors in [17]. For the new parameterizations, the parameters for the 10 % depth level are used. Because the numerical simulations for the direct components are limited to 730 nm (section 4.5), the comparison of the combined downwelling irradiance E_{d} is also carried out on a wavelength range of only 400 - 730 nm. The larger wavelength range for the comparison of the diffuse models is to be taken into account for the interpretation of the results.

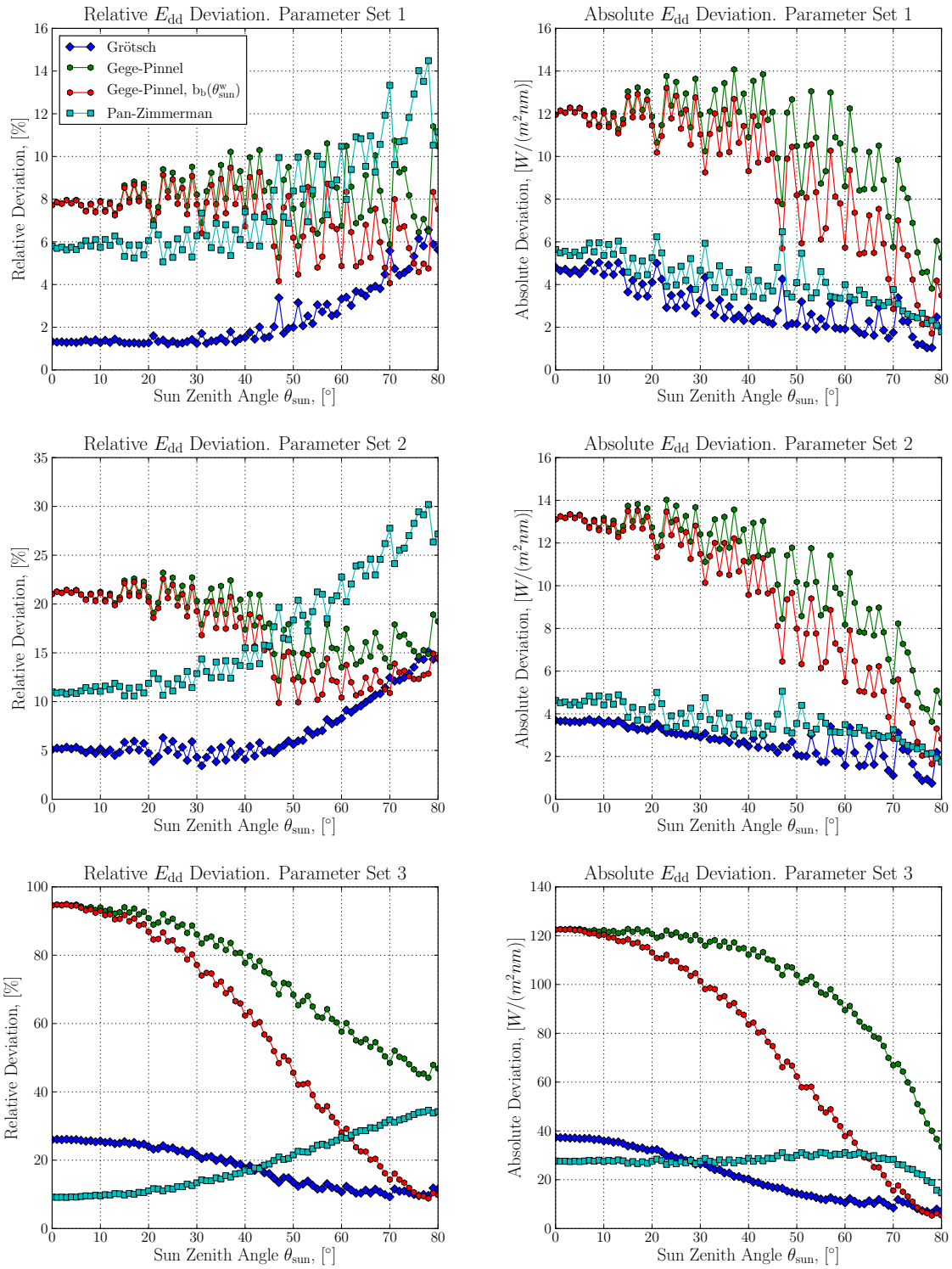

Figure 6.7: Relative and absolute deviations between Ecolight calculated and modelled E_{dd} for all parameter sets (section 4.3). The plotted values were averaged over all depths (0 - 10 m, 1 m steps) and wavelengths (400 - 730 nm, 1 nm steps).

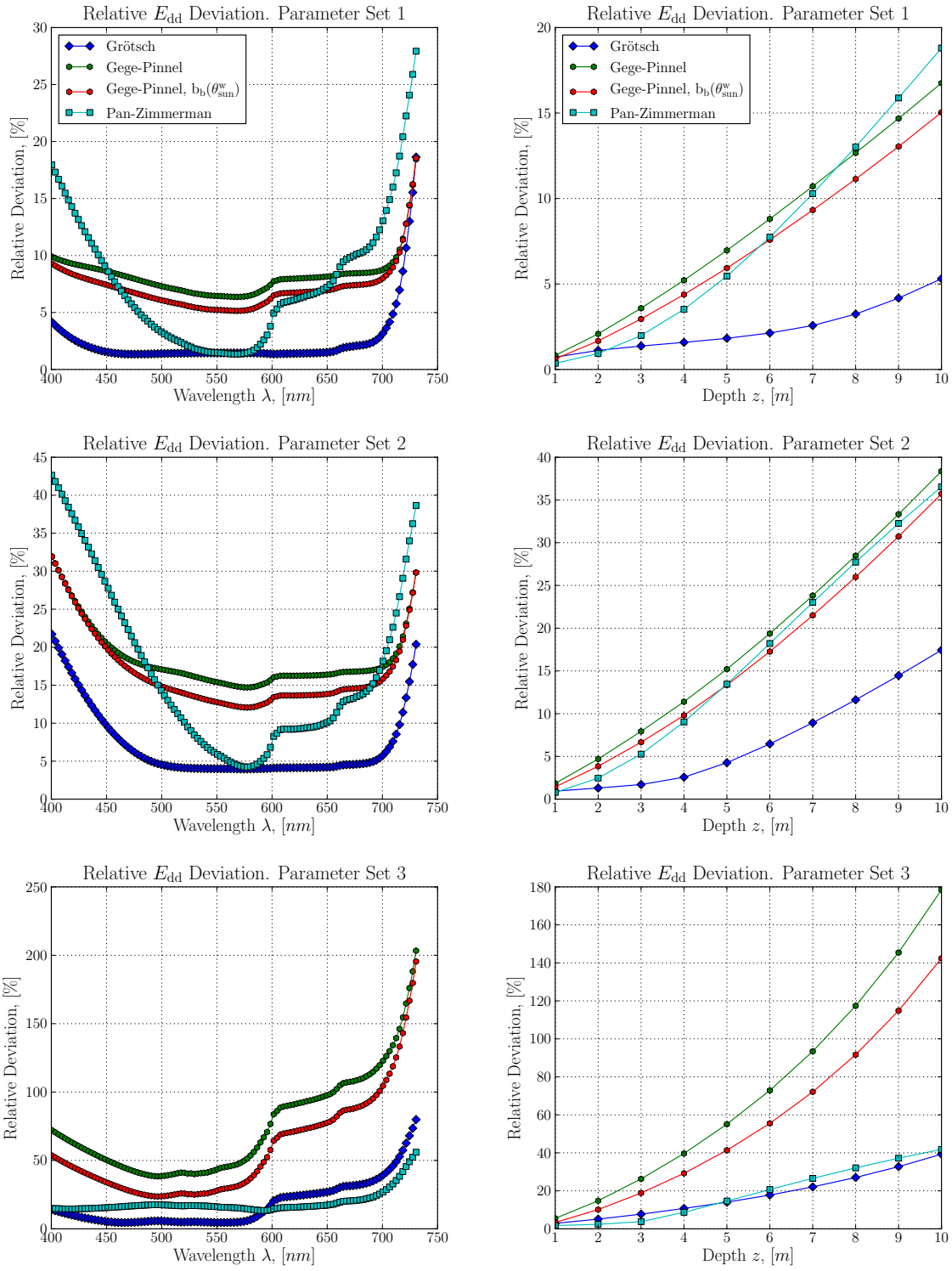

Figure 6.8: Relative deviations between Ecolight calculated and modelled E_{dd} for all parameter sets (section 4.3). On the left side, the plotted values were averaged over all depths (0 - 10 m, 1 m steps) and sun zenith angles (0 - 80°, 1° steps). On the right side, the values for all wavelengths (400 - 730 nm, 1 nm steps) and sun zenith angles were averaged.

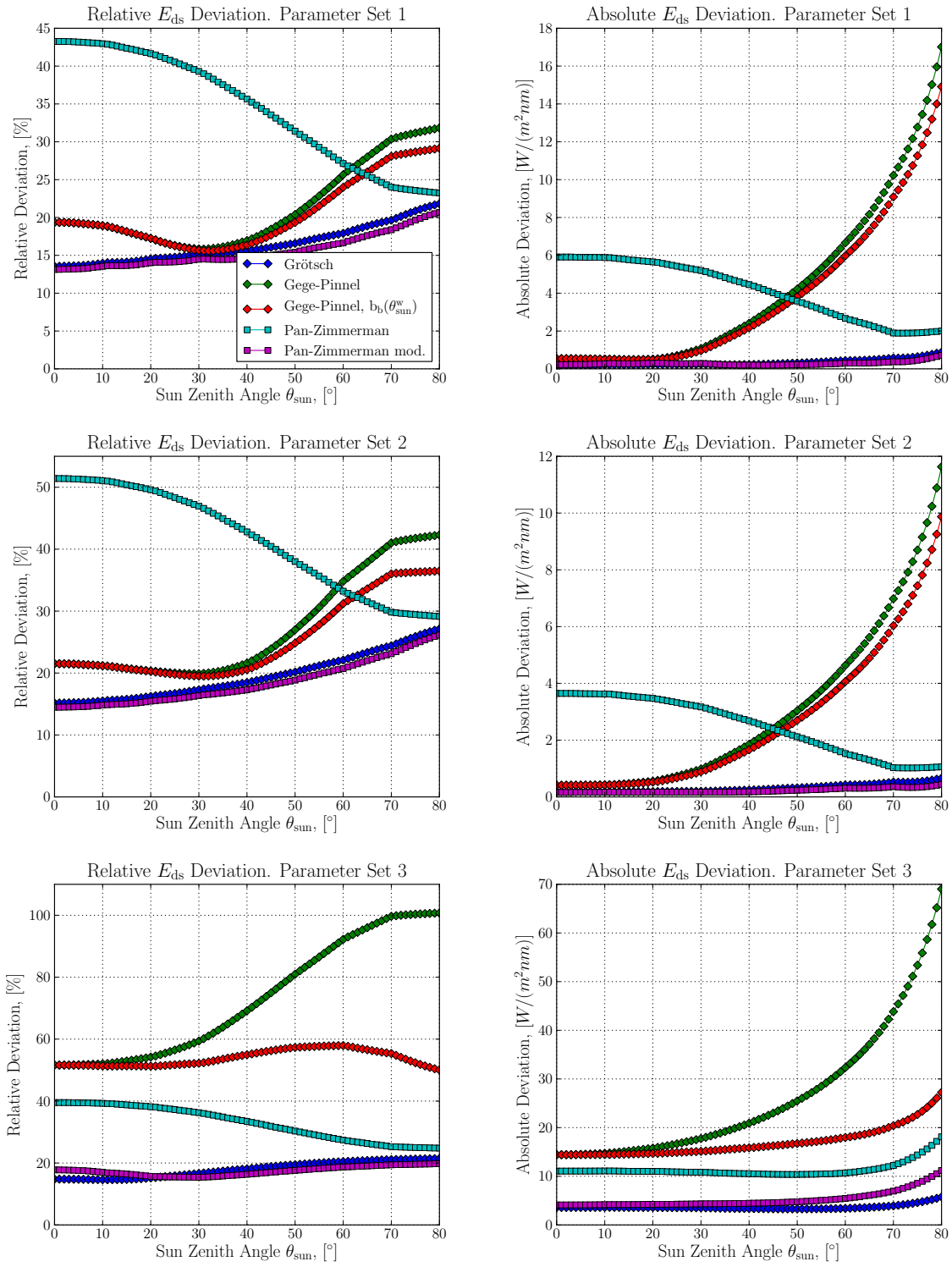

Figure 6.9: Relative and absolute deviations between Ecolight calculated and modelled E_{ds} for all parameter sets (section 4.3). The plotted values were averaged over all depths (0 - 10 m, 1 m steps) and wavelengths (400 - 830 nm, 1 nm steps).

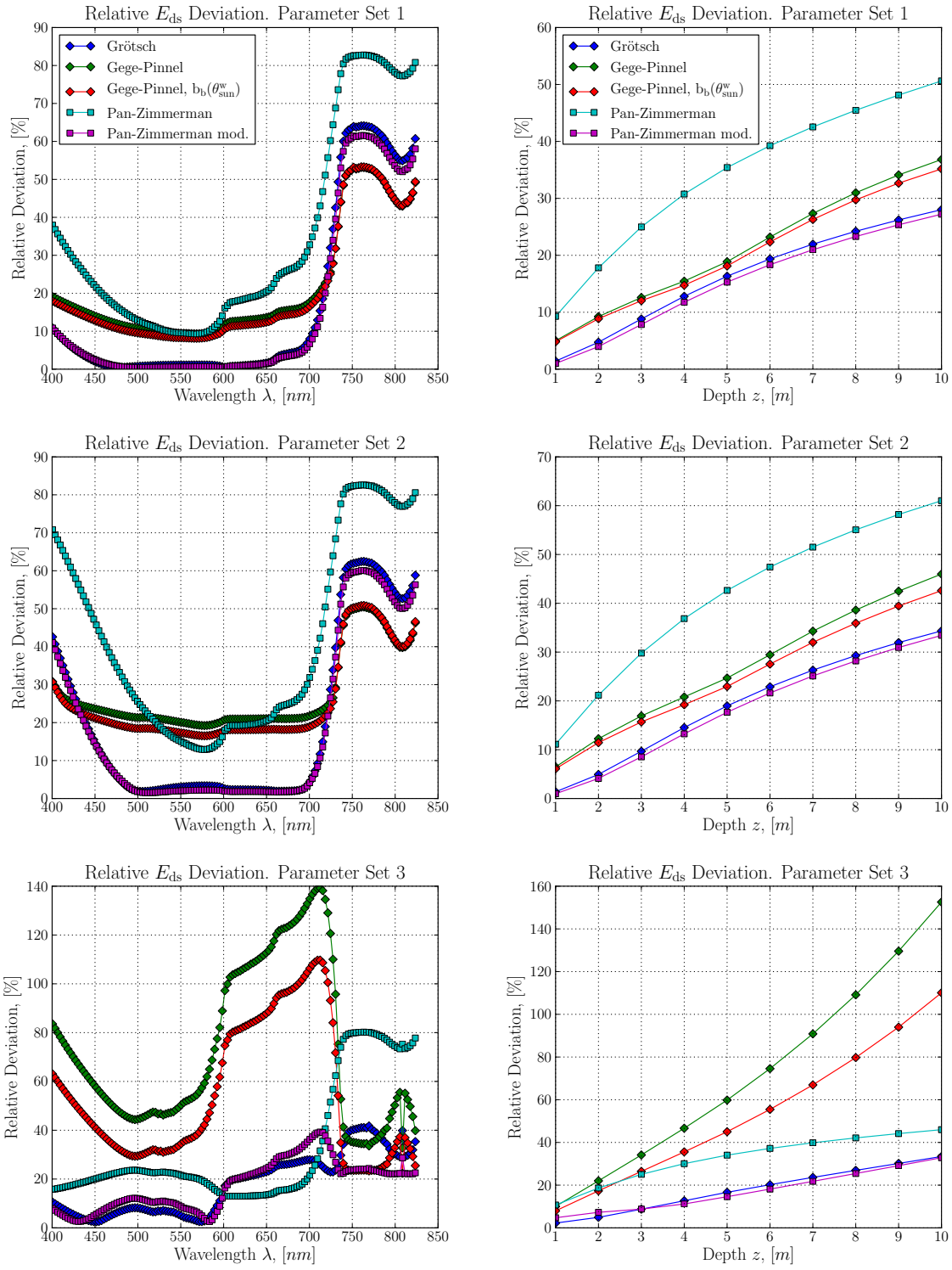

Figure 6.10: Relative deviations between Ecolight calculated and modelled E_{ds} for all parameter sets (section 4.3). On the left side, the plotted values were averaged over all depths (0 - 10 m, 1 m steps) and sun zenith angles (0 - 80°, 1° steps). On the right side, the values for all wavelengths (400 - 830 nm, 1 nm steps) and sun zenith angles were averaged.

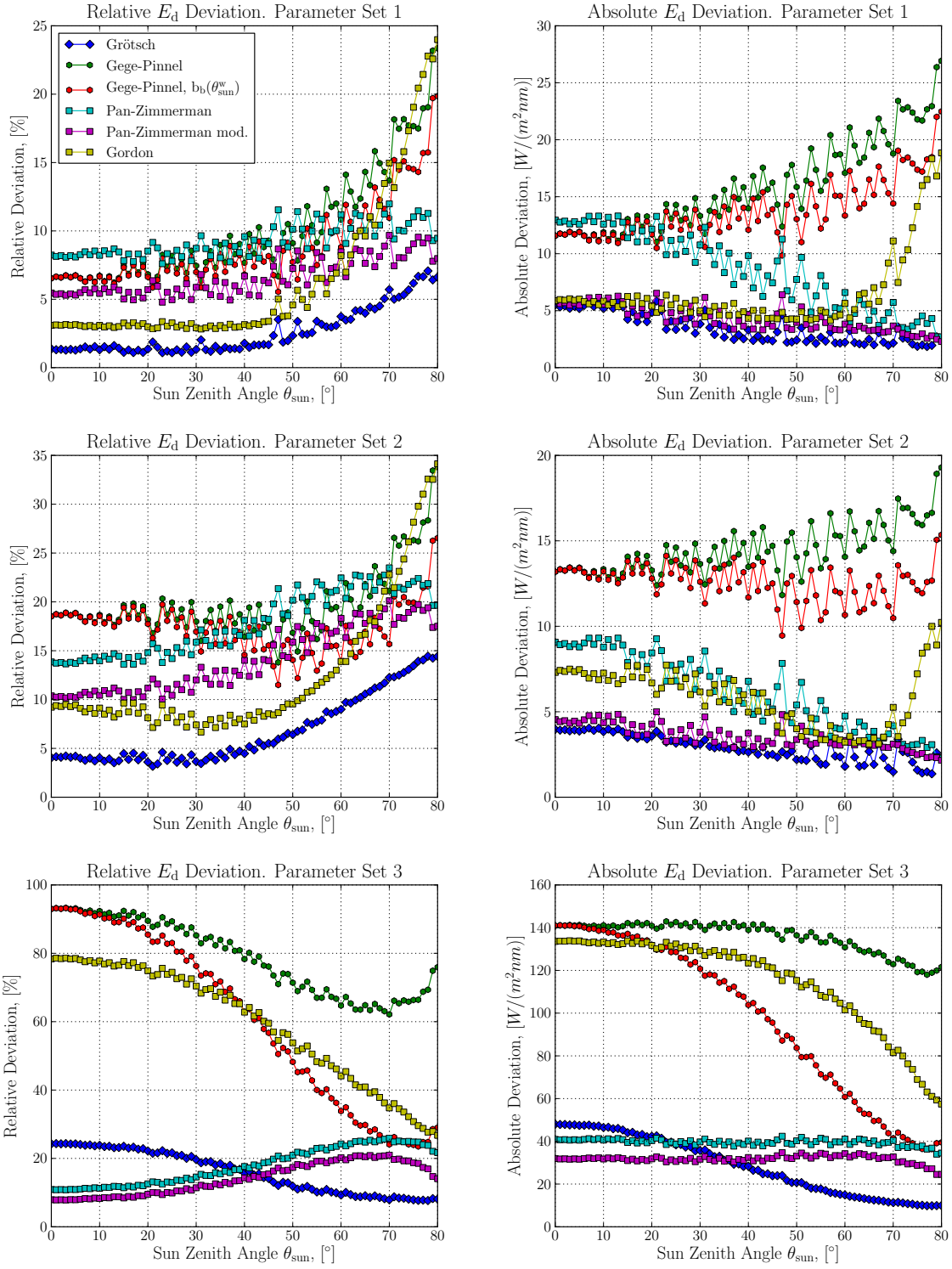

Figure 6.11: Relative and absolute deviations between Ecolight calculated and modelled E_d for all parameter sets (section 4.3). The plotted values were averaged over all depths (0 - 10 m, 1 m steps) and wavelengths (400 - 730 nm, 1 nm steps).

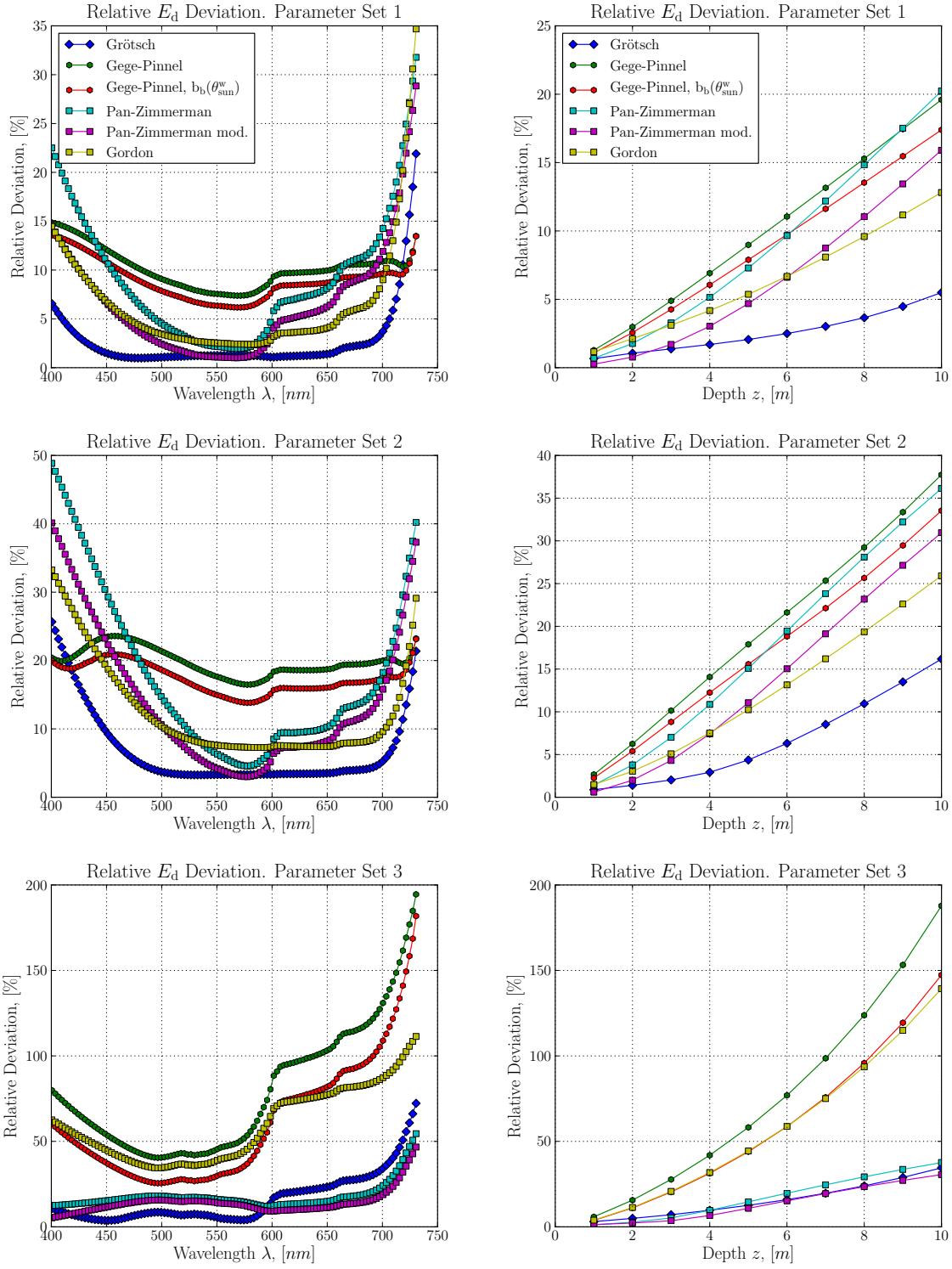

Figure 6.12: Relative deviations between Ecolight calculated and modelled E_d for all parameter sets (section 4.3). On the left side, the plotted values were averaged over all depths (0 - 10 m, 1 m steps) and sun zenith angles (0 - 80°, 1° steps). On the right side, the values for all wavelengths (400 - 730 nm, 1 nm steps) and sun zenith angles were averaged.

In table 6.1, 6.2 and 6.3, the mean (± standard deviation) and maximal, relative and absolute deviations are listed for all models and irradiances. The mean values are averages over all wavelengths, depths and sun zenith angles. The maximal values are calculated from the mean over wavelength and depth, as plotted in figures 6.7, 6.9, 6.11.

Table 6.1: Relative and absolute mean and maximal deviations for all investigated models and parameter set 1 (section 4.3).

		E_{dd}		E_{ds}		E_{d}	
		mean	max	mean	max	mean	max
Grötsch; [%],	rel.	2.40±1.46	6.56	16.39±2.36	21.82	2.60±1.70	7.07
[W/(m^{2}nm)],	abs.	3.02±1.13	5.04	0.33±0.17	0.88	3.47±1.29	5.84
Gege	rel.	8.23±1.21	11.41	21.36±5.31	31.83	10.16±4.18	23.35
	abs.	10.77±2.40	14.07	4.24±4.41	17.01	15.94±4.00	26.93
Gege, $b_{\mathrm{b}}(\theta'_{\mathrm{sun}})$	rel.	7.17±1.35	9.47	20.48±4.45	29.14	8.96±3.16	19.85
	abs.	9.26±3.12	13.21	3.79±3.87	14.91	13.85±2.60	22.49
Pan-Z.	rel.	7.80±2.43	14.49	34.43±7.24	43.26	9.26±1.16	11.98
	abs.	4.22±1.11	6.47	4.16±1.49	5.91	8.58±3.40	13.31
Pan-Z. Mod.	rel.			15.51±2.09	20.68	6.62±1.35	9.68
	abs.			0.29±0.10	0.71	4.31±1.12	6.53
Gordon '75	rel.					6.43±5.58	23.99
	abs.					6.49±3.28	18.85

Table 6.2: Relative and absolute mean and maximal deviations for all investigated models and parameter set 2 (section 4.3).

		E_{dd}		E_{ds}		E_{d}	
		mean	max	mean	max	mean	max
Grötsch; [%],	rel.	6.97±3.13	15.13	19.43±3.60	27.12	6.71±3.48	14.44
[W/(m^{2}nm)],	abs.	2.69±0.78	3.74	0.31±0.14	0.66	2.90±0.75	4.04
Gege	rel.	18.44±2.97	23.20	27.20±8.19	42.29	19.83±3.64	33.80
	abs.	10.77±2.78	14.02	3.01±2.95	11.63	14.51±1.47	19.29
Gege, $b_{\mathrm{b}}(\theta'_{\mathrm{sun}})$	rel.	16.63±4.06	22.58	25.29±6.23	36.48	17.39±2.51	26.54
	abs.	9.34±3.58	13.52	2.64±2.51	9.87	12.59±1.07	15.35
Pan-Z.	rel.	16.88±5.94	30.19	41.48±8.11	51.41	17.79±3.26	23.49
	abs.	3.61±0.77	5.06	2.50±0.97	3.65	6.10±2.19	9.31
Pan-Z. Mod.	rel.			18.39±3.42	26.12	14.08±3.31	20.12
	abs.			0.23±0.08	0.44	3.57±0.71	5.00
Gordon '75	rel.					12.46±6.94	34.13
	abs.					5.82±1.74	10.23

Table 6.3: Relative and absolute mean and maximal deviations for all investigated models and parameter set 3 (section 4.3).

		E_{dd}		E_{ds}		E_d	
		mean	max	mean	max	mean	max
Grötsch; [%],	rel.	17.94±6.03	26.10	17.96±2.51	21.43	16.03±6.12	24.34
[W/(m^{2}nm)],	abs.	21.57±10.42	37.35	3.65±0.48	5.76	28.47±13.62	48.02
Gege	rel.	74.89±17.02	94.95	72.93±18.47	100.73	78.96±10.75	93.31
	abs.	102.22±24.43	122.79	26.34±13.62	69.03	135.88±7.21	142.95
Gege, $b_b(\theta'_{sun})$	rel.	57.95±30.02	94.86	53.85±2.52	57.92	60.75±25.18	93.22
	abs.	75.38±40.02	122.64	16.92±2.96	27.23	96.96±36.69	141.10
Pan-Z.	rel.	18.95±8.48	34.62	32.78±5.34	39.52	17.81±5.33	25.97
	abs.	27.57±2.96	31.15	11.36±1.52	18.10	39.52±1.52	42.37
Pan-Z. Mod.	rel.			17.39±1.42	19.76	14.04±4.60	20.99
	abs.			5.21±1.61	11.18	31.65±1.80	34.69
Gordon '75	rel.					59.38±16.76	78.64
	abs.					114.62±21.98	133.88

6.4 WASI-Fits of sensor depth

The parameterizations for $\overline{K}_{dd}$ and $\overline{K}_{ds}$ (equations (6.1) and (6.3)) were implemented into WASI [5]. The fit of the models to the field measurements (table 5.1) was carried out as desribed in section 5.6. In figure 6.13 and 6.14, the fitted sensor dephts are plotted against independent measurements of the sensor depth for the Grötsch and Gordon '75 model. Each point in the graph corresponds to one measurement, consisting of several data takes (usually 30). The median[2] of those data takes is plotted with the standard deviation as errorbars. The atmospheric parameters were determined by fitting the atmospheric model in WASI[3] to the measurements above the water. For the measurements with an additional above water irradiance sensor, the mean fit result over all measurements has been used. The results of those fits are printed in table 6.4. In tables 6.5 and 6.6, the absolute and relative standard deviations as well as the absolute and relative deviations from the independent sensor depth measurement are printed for the Grötsch and Gordon '75 model, respectively.

Table 6.4: Atmospheric parameters derived with WASI from above water measurements.

	M1	M2	M3	L1	L2
H_{oz}, [cm]	0.276	0.662	0.337	0.225	0.535
α, [-]	-0.170	0.070	-0.207	0.522	0.038
β, [-]	0.455	1.598	0.461	0.226	1.837
WV, [cm]	0.157	1.977	0.804	0.659	1.103

[2]The median instead of the mean was used to be less dependent on outliers.
[3]Which is the Gregg and Carder 1990 model [9], but with the separation of direct and diffuse irradiances, as described in chapter 3.

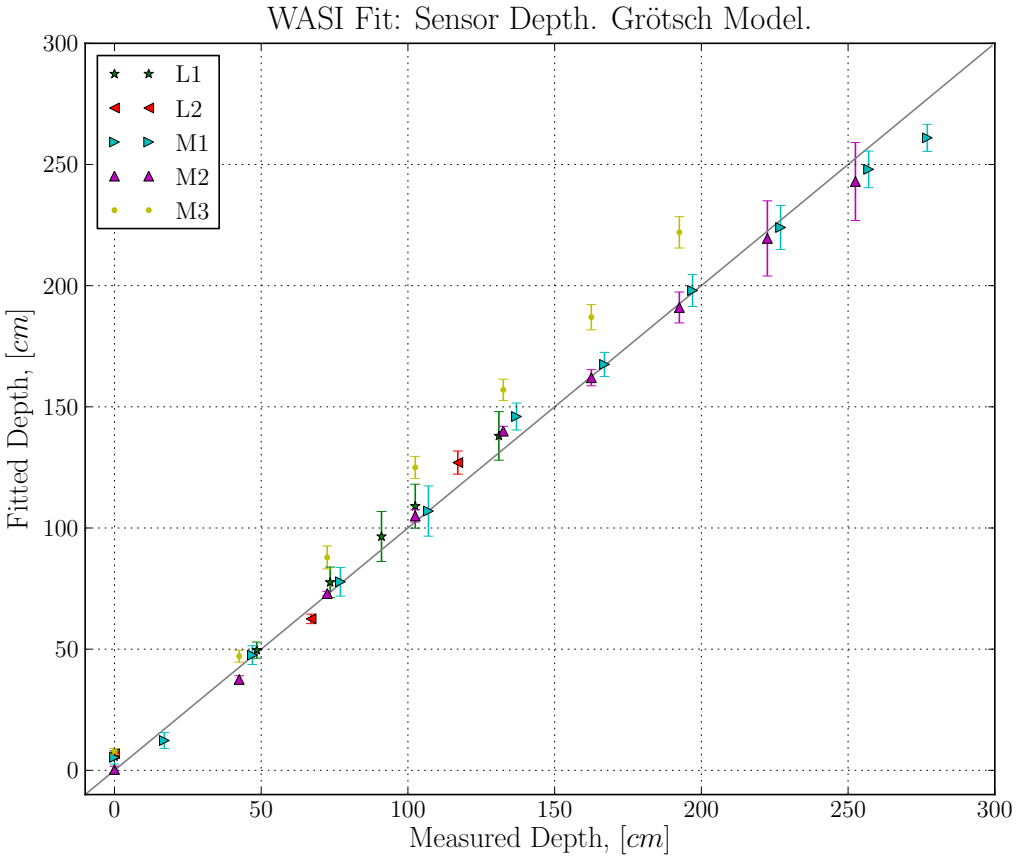

Figure 6.13: Validation of WASI fits: Fit results for sensor depth plotted against measured sensor depth, Grötsch model.

Table 6.5: Statistics to the WASI fit results for the Grötsch attenuation model.

Site	abs. STD, [cm]	rel. STD, [%]	abs. dev., [cm]	rel. dev., [%]
L1	6.58	8.65	4.99	5.12
L2	2.62	3.51	4.13	0.92
M1	5.95	6.41	-1.41	-2.87
M2	5.51	3.44	-0.97	-1.16
M3	4.14	4.45	18.40	17.14
Abs. mean	4.96	5.29	5.98	5.44

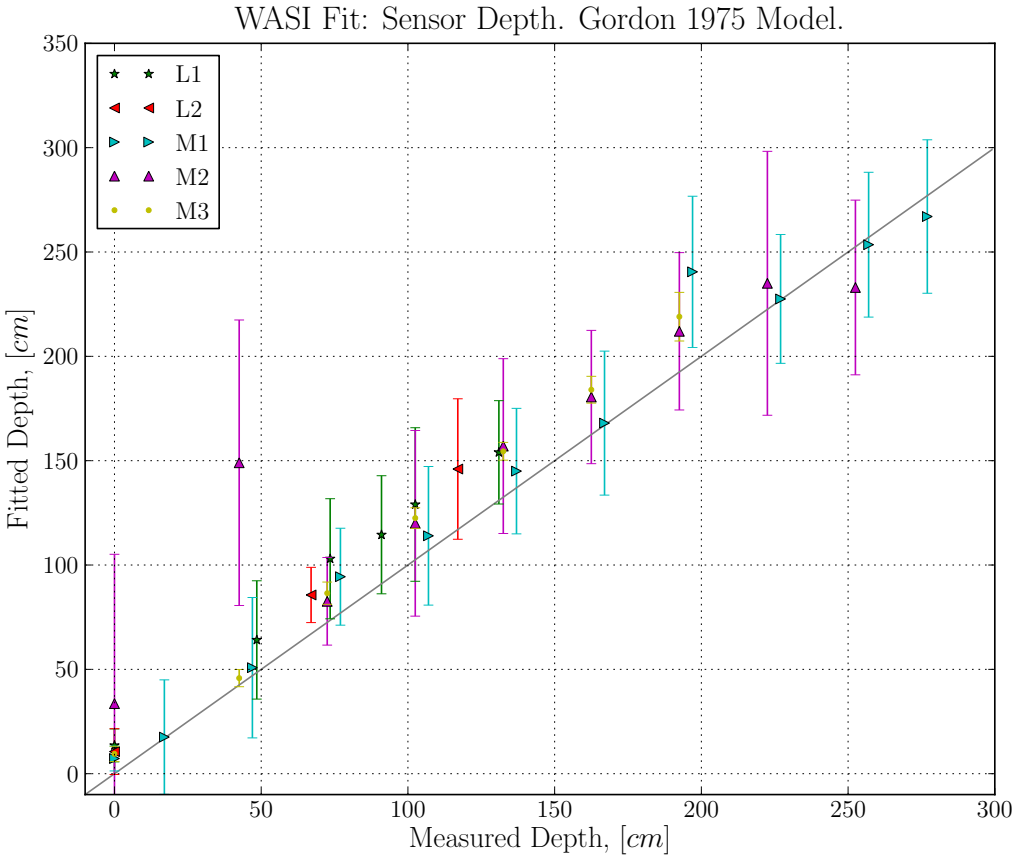

Figure 6.14: Validation of WASI fits: Fit results for sensor depth plotted against measured sensor depth, Gordon '75 model.

Table 6.6: Statistics to the WASI fit results for the Gordon '75 attenuation model.

Site	abs. STD, [cm]	rel. STD, [%]	abs. dev., [cm]	rel. dev., [%]
L1	25.81	36.70	21.94	28.31
L2	19.29	24.26	19.42	26.31
M1	29.69	39.54	6.87	6.42
M2	46.90	43.65	24.74	39.90
M3	5.76	5.85	16.69	15.03
Abs. mean	25.49	30.00	17.93	23.19

7 Discussion

The discussion follows the same scheme as the results: first the simulations of K_{dd} and K_{ds} are explained, followed by the parameterizations. The main part is the discussion of the comparison between new and existing parameterizations. The verification of the new model with field measurement data is the last part of the discussion.

7.1 Simulations of K_{dd} and K_{ds}

It is obvious that the direct and diffuse components in the downwelling irradiance differ spectrally, as shown in figure 3.1. But a main question for the justification of the new analytical model is: how different is the change with depth of the downwelling irradiance's direct and diffuse components? This question immediately leads to the downwelling attenuation coefficient, as E_{d} and K_{d} are linked by equation (2.7). In chapter 3, the parameterizations for K_{dd} and K_{ds} in the Gege-Pinnel model[1] [6] differ by the path length correction. To validate and optimize this approach, numerical simulations were carried out.

The simulated direct and diffuse irradiances confirmed that a separate parameterization of K_{dd} and K_{ds} is needed to account for the deviant behavior of E_{dd} and E_{ds}. In section 6.1, upper panel of figure 6.1, it is obvious that the approximation of K_{dd} as $(a + b_{\mathrm{b}})/\cos(\theta^{\mathrm{w}}_{\mathrm{sun}})$ works quite perfectly for a sun at zenith position. The spectral shape can be reproduced and there is nearly no depth dependency visible. At the lower panel of figure 6.1, the situation at a sun zenith angle of 80° is shown. Just below the water surface, the approximation is still valid over the whole range of attenuation values. For increasing depths, the approximation tends to overestimate K_{dd}. The effect is more pronounced at higher attenuation values and leads to a non linear relationship between $(a + b_{\mathrm{b}})/\cos(\theta^{\mathrm{w}}_{\mathrm{sun}})$ and the calculated K_{dd}.

This is most likely due to the effects of multiple scattering, which is not included in the simple approximation. For increasing depths, also the fraction of photons which were scattered multiple times, increases: each scattering event increases the path length of a photon through

[1] the notation for the Gege-Pinnel model in this work differs slightly from the one in [6]: the path length correction for the direct component is included in the K_{dd} parameterization instead of the E_{dd} exponent.

the water column to reach a certain geometrical depth and an increased path length leads to higher absorption and scattering probabilities.

For K_{ds} the situation is more complicated. The simple geometric path length amplification with the $1/\cos\theta^{\mathrm{w}}_{\mathrm{sun}}$-factor isn't valid for the diffuse irradiance because the diffuse above water light field distribution has a much more homogeneous distribution (in comparison to the above water direct light field) which can be approximated as cardioidal: the highest intensities are still observed at the sun's direction, but the remaining intensity from off-sun directions has the same order of magnitude [10]. This is the reason why in the right part of figure 6.2, K_{ds} is plotted as a function of only $(a + b_{\mathrm{b}})$. For both sun positions, zenith and 80°, this approximation underestimates K_{ds}. The depth dependency is lower for the zenith case, but the tendency is the same: for values just below the water surface, the relationship is quite linear but shows the highest offset. For increasing depths, the offset becomes smaller, but the relationship is less linear. An additional $1/\cos(\theta^{\mathrm{w}}_{\mathrm{sun}})$-factor would lead to a change from underestimation to overestimation of K_{ds} with increasing sun zenith angle (figure 6.2, lower left plot).

7.2 New Parameterization of K_{dd} and K_{ds}

The simulations clearly show the necessity of a separate parameterization for K_{dd} and K_{ds}. The Pan and Zimmerman [17] model offers a distinct parameterization. However, the authors couldn't adjust their parameterizations to E_{dd} and E_{ds} separately as Hydro-/Ecolight doesn't support a partitioned calculation: to simulate E_{ds}, a sun zenith angle of 89°, as a quasi diffuse setup, was chosen. With their workaround, the sun zenith dependency of K_{ds} couldn't be taken into account. The sun zenith parameterization of $\overline{K}_{\mathrm{dd}}$ in the Pan and Zimmerman model is also problematic as the numeric simulations were performed with a 10° quad-discretization in Hydro-/Ecolight. In section 4.5 it has been shown that this 10° discretization can lead to large errors in E_{dd} and consequently also in the parameterization of the sun zenith dependency in K_{dd}.

For this study, E_{dd} and E_{ds} were simulated separately, using a modified version of Ecolight. In addition, E_{dd} was simulated with a 2° quad-resolution. To find a physical and simple parameterization for K_{dd} and K_{ds} and to compare its performance with the semi-analytical model of Pan and Zimmerman, was a main task in this work. To show the potential of the modified Hydro-/Ecolight version, the parameterization for K_{ds} in the Pan and Zimmerman model was modified to account for the sun zenith angle dependency. This modified version of the model was also included into the comparison.

7.2.1 Sun Zenith Angle dependent Backscattering Coefficient

In figure 6.3, the ratios of $K_{\mathrm{dd}}(0^-)$ and $K_{\mathrm{ds}}(0^-)$ to a, $a + b_{\mathrm{b}}$, $a + \overline{b_{\mathrm{b}}}$ and $a + b_{\mathrm{b}}(\theta^{\mathrm{w}}_{\mathrm{sun}})$ at a sun zenith angle of 80° are plotted. For the direct component, it is obvious that the $a + b_{\mathrm{b}}(\theta^{\mathrm{w}}_{\mathrm{sun}})$ approximation removes the dependency on attenuation almost perfectly whereas the other models leave a certain part of the dependency unresolved. Towards high attenuation values the models converge to a certain offset. The reason is that high attenuation values in the used water constituent set 1 (section 4.3) are absorption dominated and therefore the backscattering parameterization is from low importance in those regions. The value of the offset is due to the longer geometrical path length at 80° sun zenith angle and can be corrected by a $1/\cos(\theta^{\mathrm{w}}_{\mathrm{sun}})$ factor, as used in the lower right plot of figure 6.1.

For $K_{\mathrm{ds}}(0^-)$ the situation is similar but there are two main differences: the $a + b_{\mathrm{b}}(\theta^{\mathrm{w}}_{\mathrm{sun}})$ approximation leads to a slight overestimation of attenuation at low attenuation values and the offset is lower than predicted by a $1/\cos(\theta^{\mathrm{w}}_{\mathrm{sun}})$-factor. The reason for both effects is the difference in light field distribution for the direct and diffuse irradiance. The assumption for the parameterization of $b_{\mathrm{b}}(\theta^{\mathrm{w}}_{\mathrm{sun}})$ is that only photons originating from the direction of the sun disc are scattered. The diffuse light field distribution of the sky can be approximated as cardioidal [10]. Still, the maximum of the diffuse radiation originates from the sun disc's direction and this is why $b_{\mathrm{b}}(\theta^{\mathrm{w}}_{\mathrm{sun}})$ is a reasonable approximation also for the diffuse light field. Also the lower offset can be explained by the diffuse light field distribution, as for any sun zenith angle photons from other directions lead to a modified mean path length. As the light field distribution in the water column becomes increasingly homogeneous with depth, the original direction of the photons is from low importance at high optical depths. In this study, a parameterization for depth-averaged $\overline{K}_{\mathrm{dd}}$ and $\overline{K}_{\mathrm{ds}}$ was developed and therefore the mean value of $b_{\mathrm{b}}(\theta^{\mathrm{w}}_{\mathrm{sun}})$ over all sun zenith angles is used.

7.2.2 Parameterization of $\overline{K}_{\mathrm{dd}}$

The developed parameterization of $\overline{K}_{\mathrm{dd}}$ (equation (6.1)) is comparable to Gordon's '75 K_{d} model (equation (2.19)) if scattering is neglected: the $1/\cos(\theta^{\mathrm{w}}_{\mathrm{sun}})$ factor corrects for the geometrical path length and l_a corresponds to κ_0. If no scattering is present, this equation is valid for all depths. However, scattering is present in natural water bodies and therefore Gordon made clear that his model is only valid just below the water surface where scattering hasn't changed the underwater light field distribution yet. For this study a parameterization of K_{dd} that can be used not only near the surface, but down to the lower border of the euphotic zone, was desired. The study of numerically calculated K_{dd} showed that a geometrical path length factor, applied to a sum of the absorption and scattering related part of the

parameterization (e.g. similar to Gordon's $\kappa_0 \cdot (a + b_\mathrm{b})$), is not leading to a water constituent independent solution.

This can be explained by the different behavior of absorption and scattering with sun zenith angle. The sun zenith angle dependency of absorption can be described by a purely geometrical factor ($1/\cos(\theta^\mathrm{w}_\mathrm{sun})$) and a small factor for the prolonged path length due to a changed light field distribution. Scattering is much more sensitive to the change of the light field distribution due to its dependency on the scattering phase functions. For K_dd just below the water surface, where the light field distribution is still unaffected by scattering, the coefficient $b_\mathrm{b}(\lambda, \theta^\mathrm{w}_\mathrm{sun})$ instead of $\overline{b_\mathrm{b}}(\lambda)$ would be the physically correct description. But for a depth averaged K_dd, $\overline{b_\mathrm{b}}(\lambda)$ turned out to be the better-suited parameter, as explained above. Only by using $\overline{b_\mathrm{b}}(\lambda)$ it was possible to obtain a water constituent independent parameterization. The increase of the parameter l_b, from the 10 % to the 1 % light level, reflects the increasingly diffuse light field with depth.

In figure 6.4, the average ratio between the numerically simulated and modeled $\overline{K}_\mathrm{dd}$ is plotted for the 10 % and 1 % light levels. A striking feature of the model is clearly visible: it performs equally well for all simulated water bodies, which cover a wide range of absorption to scattering ratios (see figure 4.1, lower right plot). The plots show quite scattered results, which is most likely due to numerical limits of Hydro-/Ecolight even though a 2° quad-discretization was used for the calculations. A more precise investigation concerning the sun zenith angle dependency of K_dd is not feasible with the existing numerical approach of Hydro-/Ecolight.

7.2.3 Parameterization of $\overline{K}_\mathrm{ds}$

In the parameterization of $\overline{K}_\mathrm{ds}$, the sun zenith angle dependency is not separately formulated for absorption and scattering. The dependency is described by $l_\theta(\theta^\mathrm{w}_\mathrm{sun}, m, n)$ (equation (6.2)). As mentioned before, the diffuse part of the Pan-Zimmerman model [17] could not be adjusted to varying sun zenith angles because the authors had no possibility to simulate the corresponding diffuse irradiances. In this study this was made possible by a modified version of Ecolight, as described in section 4.2. To compare the newly developed parameterization by fair means with the Pan-Zimmerman model, the sun zenith parameterization $l_\theta(\theta^\mathrm{w}_\mathrm{sun}, m, n)$ has been adapted for both models. However, for each model the parameters m and n were adjusted separately. Of course, the sun zenith angle dependency could have been implemented into Pan-Zimmerman model's polynomial description, with probably better results. But the intention behind the modified Pan-Zimmerman model was to show the possibilities for future research with the developed Ecolight modification. Also the fact that no water constituent independent parameter set could be found for the modified Pan-Zimmerman model shows that this solution is just an intermediate step.

In figure 6.5, the sun zenith dependency of the two models is plotted together with the fit of $l_\theta(\theta^{\mathrm{w}}_{\mathrm{sun}}, m, n)$ for both depth average levels. For the Grötsch model the fit results for the three different water constituent concentration sets (section 4.1) are very similar. For this reason, the mean values of the fit parameters of each depth average level were chosen for the final result. However, m and n are slightly dependent on the depth average level. For the modified Pan-Zimmerman model an universal solution for absorption and scattering dominated water bodies could not be found.

Apart from $l_\theta(\theta^{\mathrm{w}}_{\mathrm{sun}}, m, n)$, the parameterization of the Grötsch model (equation (6.3)) consists of three elements: absorption coefficient $a(\lambda)$, sun zenith averaged backscattering coefficient $\overline{b_{\mathrm{b}}}(\lambda)$ and a term which is attributed to multiple scattering. The reason why $\overline{b_{\mathrm{b}}}(\lambda)$ is used instead of $b_{\mathrm{b}}(\theta^{\mathrm{w}}_{\mathrm{sun}}, \lambda)$ has already been explained. Additionally, a water constituent concentration independent solution was only possible with the use of $\overline{b_{\mathrm{b}}}(\lambda)$ in combination with the multiple scattering term. This term consists of a scale factor l_{ms}, $\overline{b_{\mathrm{b}}}(\lambda)$ and the cosine of the sun zenith angle in water. The light field becomes increasingly diffuse with depth, as photons can be scattered multiple times within the watercolumn. However, for the calculation of $\overline{b_{\mathrm{b}}}(\lambda)$, the probability distributions for single-scattering are included. The probability that a photon is scattered multiple times within the watercolumn, increases with depth. Though a correction for this effect should be increasing with depth as well, which is the case for l_{ms} at the two investigated depth levels. The correction must also be related to the concentration of scattering particles, which is why $\overline{b_{\mathrm{b}}}(\lambda)$ is included. For a sun at the horizon the light field is already nearly homogeneous and as scattering can only increase the homogeneity of a light field distribution, the correction for multiple scattering decreases with sun zenith angle.

In figure 6.6, the ratio between the numerically simulated and modeled $\overline{K}_{\mathrm{ds}}$ is plotted. K_{ds} is averaged to the 10 % and 1 % light levels and all wavelengths. The results are much less scattered than the corresponding plot for the $\overline{K}_{\mathrm{dd}}$ model but still show slight relicts of the 10° quad size used in Ecolight for the calculation of E_{ds}. The relatively steep drop at 70° can also be observed in the plots of l_θ (figure 6.5) and is most likely due to a numerical approximation in Ecolight concerning the polar caps used in the quad-layout. The fact that the Grötsch and the modified Pan-Zimmerman models perform very similar, indicates that the numerical limits of Ecolight were reached. Nevertheless, the sub-percent absolute deviations for all concentration sets, sun zenith angles and models are remarkable. It has to be kept in mind that for the modified Pan-Zimmerman model, two parameter sets are used for $l_\theta(\theta^{\mathrm{w}}_{\mathrm{sun}}, m, n)$, whereas the Grötsch model shows an equal performance with only one set.

7.3 Comparison

To visualize differences between multidimensional datasets, averaging over certain dependencies is necessary. The models for E_{dd}, E_{ds} and the combined models for E_{d} are primarily dependent on three variables: wavelength, depth and sun zenith angle. To show a model's performance concerning one of them, the other two have to be averaged. The relative deviations are calculated dependent on all three variables. For the sun zenith dependency, also the absolute deviations are calculated. As absolute deviations are strongly dependent on the mean intensity level, which is highly variable with wavelength and depth, they are of little significance for the evaluation of those dependencies. The mean intensity level also decreases with sun zenith angle but in a moderate and consistent manner. However, a general trend towards lower absolute deviations with increasing sun zenith angles has to be expected for the interpretation of those plots.

7.3.1 E_{dd} models

In figure 6.7, the relative deviations for the E_{dd}-models are plotted on the left side. The results for the absorption dominated parameter sets 1 and 2 are qualitatively quite similar. However, the deviations are significantly increased for set 2 and even more for the scattering dominated set 3. The most relevant water constituent concentrations for this study are realized in set 1. The relative deviations of the Grötsch model are constantly below 2 % up to a sun zenith angle of about 50° and below 4 % up to about 70°, which is the usual limit in sun zenith angle for field measurements. But also the highest relative deviation of 6.56 % at a sun zenith angle of 80° (table 6.1) is still tolerable. The Gege-Pinnel models and the Pan-Zimmerman model show similar average relative deviations (8.24 %, 7.17 % and 7.80%) compared to 2.40 % of the Grötsch model. The absolute deviation plots clearly show the expected decreasing trend towards higher sun zenith angles. Remarkable is the similar performance of the Pan-Zimmerman and Grötsch model in this representation. The effect of $b_{\mathrm{b}}(\theta^{\mathrm{w}}_{\mathrm{sun}}, \lambda)$ in the Gege-Pinnel model is visible for each parameter set, most clearly though for the scattering dominated set 3: for low sun zenith angles, the models show similar performances, as $b_{\mathrm{b}}(\theta^{\mathrm{w}}_{\mathrm{sun}} = 0°, \lambda) = b_{\mathrm{b}}$. Towards higher sun zenith angles the positive effect increases. As $b_{\mathrm{b}}(\theta^{\mathrm{w}}_{\mathrm{sun}}, \lambda)$ is a scattering related quantity, its effect is most obvious for highly scattering water compositions, as described by parameter set 3.

In figure 6.8, the relative deviations for the E_{dd}-models with wavelength and depth are shown for each parameter set. The deviations with wavelength of the Grötsch model for the most relevant parameter set 1 are below 2.5 % for wavelengths between 450 nm and 700 nm. Towards higher wavelengths, the deviation increases rapidly. The Pan-Zimmerman

model shows a much more pronounced dependency on wavelength, whereas the Grötsch and Gege-Pinnel models are only weakly dependent on wavelength. The deviations are contiguously increasing with depth for all models. However, for the depth dependency, the Grötsch model shows significantly better results than the remaining models, except for parameter set 3, where the Pan-Zimmerman model is competing.

In summary, the newly developed Grötsch model is superior to the Gege-Pinnel and Pan-Zimmerman models for the absorption dominated sets 1 and 2. For the scattering dominated set 3, the Pan-Zimmerman model performs similarly. The positive effect of $b_{\mathrm{b}}(\theta^{\mathrm{w}}_{\mathrm{sun}}, \lambda)$ for the Gege-Pinnel model is visible for all investigated dependencies.

7.3.2 E_{ds} models

In the comparison of the E_{ds} models, concerning sun zenith angles (figure 6.9), the sun zenith corrected Pan-Zimmerman model is included. The original Pan-Zimmerman model performs reasonably well only at very high sun zenith angles. The modified Pan-Zimmerman model performs similar to the Grötsch model for all parameter sets. The mean relative deviation for both models ist not correlated to the parameter set and is on the order of 15-20 % (tables 6.1, 6.1 and 6.1). It has to be pronounced that only one set of model parameters m, n for the shared sun zenith dependency $l_\theta(\theta^{\mathrm{w}}_{\mathrm{sun}}, m, n)$ was used within the Grötsch model, whereas for the modified Pan-Zimmerman model, a second model parameter set had to be used for the scattering dominated case 3. The effect of the $b_{\mathrm{b}}(\theta^{\mathrm{w}}_{\mathrm{sun}}, \lambda)$ correction for the Gege-Pinnel model is clearly visible and becomes more pronounced towards more scattering dominated sets, as it is the case for the E_{dd} model.

In figure 6.10, the relative deviations for the E_{ds}-models with wavelength and depth are shown for each parameter set. Also for those dependencies, the modified Pan-Zimmerman and the Grötsch model perform very similarly. For parameter set 1, the maximal relative deviation for both models at wavelengths between 450 nm and 650 nm is below 2.5 % and increases dramatically for wavelengths above 700 nm. For parameter set 2, the same observation is true but with increasing deviations already below 500 nm. The relative deviations with depth are contiguously increasing for all models and parameter sets. The modified Pan-Zimmerman and the Grötsch models show similar performances for all parameter sets, with maximal relative deviations at a depth of 10 m of about 30 %. From the wavelength dependent plot it is clear that those high deviations mainly originate from wavelengths above 700 nm. As the combined comparison is carried out on a wavelength range of only 400-730 nm, due to numerical limitations in the simulations of the direct irradiance, those high relative errors are not influencing the combined model results.

7.3.3 E_d models

As the plots in figure 6.11 are calculated with the combined E_{dd} and E_{ds} models, the observations for the separate models are still valid for the combined models. The E_d model of Gordon was included in the comparison and performs well in the chosen wavelength and depth ranges. Only for the scattering dominated set 3 it performs considerably worse than the Grötsch and Pan-Zimmerman models. The Grötsch model has a mean relative deviation of 2.60 % (table 6.1) for the parameter set 1.

In figure 6.12, the relative deviation's wavelength and depth dependencies for all models are shown. For the parameter set 1, a relative deviation of below about 2.5% at wavelengths between 450 nm and 700 nm for the Grötsch model are achieved. The mean relative deviation over all wavelengths and sun zenith angles also stays below 2.5 % for depths up to six meters, whereas the best compared models already show a relative deviation of about 7 % at this depth. For the scattering dominated case 3, the Pan-Zimmerman and modified Pan-Zimmerman models perform comparable to the Grötsch model at mean relative deviations of about 14-18 % (table 6.3).

In summary it can be stated that the newly developed parameterizations for K_{dd} and K_{ds} in the Grötsch model perform better than the compared models under almost all investigated circumstances.

7.4 WASI-Fits of sensor depth

The new analytical model, including the Grötsch models for K_{dd} and K_{ds}, are fitted to field measurements using WASI. The result of the model parameter sensor depth is compared to independent measurements to show the validity of the new analytical approach: the correct treatment of wave-focusing induced effects cannot be shown through numerical calculations with Hydro-/Ecolight, as only wave-slope statistics are included in the code. Because the measurements were performed at relatively shallow depths of maximal 2.8 m, a reliable comparison of K_{dd} and K_{ds} models cannot be carried out. For this reason, only the comparison of the conventional and widely used Gordon model to the newly developed analytical model is presented.

In figure 6.14, the sensor depth obtained by fitting the Gordon '75 model is plotted against independently measured values and the corresponding statistics are printed in table 6.6. The tendency for all measurement sets[2] is generally towards overestimation of sensor depth. The measurements M2 were obtained under completely overcasted conditions, therefore the wave

[2] for details about the measurement sets, see table 5.1

focusing effect is unlikely to have caused the two outliers at small depths. Most likely this is due to a wrong estimation of the atmospheric parameters in the preceding fit of the Gregg and Carder model[3]. The fit of the Gordon model cannot compensate these errors through the fit parameters f_{dd} and f_{ds}, as the new model could. Measurement M3 was performed at perfectly clear sky conditions but very high sun zenith angles. The fit for the M3 measurements yields results similar to the other measurements. A measure for the influence of the wave-focusing effect is the standard deviation (STD) of the fit results. The Gordon '75 model shows relatively large STDs at all depths, a dependency is not clearly visible. The measurement M3 shows very small STDs, probably as a nearly completely diffuse light field at high sun zenith angles leads to the suppression of wave-focusing effects. However, the fit results for measurements M2 and M3 which were performed at cloudy conditions, don't support this statement.

The fit results for the Grötsch model are plotted in figure 6.13 and the corresponding statistics are printed in table 6.5. A clear discrimination of the different measurement conditions through the fit results is not possible, except for the measurement M3, which was carried out with the sun next to the horizon. Here a clear overestimation of sensor depth is persistent. A reason for this could be the fit for the yellow substance exponent S. The fit of sensor depth is slightly dependent on this parameter and for such extreme sun zenith angles, the determination of S through the fit to measurements is problematic. Also the limited sensitivity of the used sensor forces the fit algorithm to estimate the sensor depth over a smaller wavelength interval, in comparison to measurements at intermediate sun zenith angles and correspondingly higher average intensities. Therefore the higher absolute and relative deviation for the measurement M3 isn't necessarily due to the description of the sun zenith angle dependency.

The absolute and relative STDs of 4.96 cm and 5.29 % for the Grötsch model in comparison to 25.49 cm and 30.00 % for the Gordon model show clearly the success of the correction for the wave focusing effect in the new analytical model. Also the absolute and relative deviations of 5.98 cm and 5.44 % in comparison to 17.93 cm and 23.19 % indicate that the physical mechanisms are correctly treated in the developed model. If the untypical case M3 is excluded from the comparison, an average absolute and relative deviation of 2.88 cm and 2.52 % is achieved. This is close to the error of the independent depth measurements. Especially the constantly low STDs and the equally good results for measurements with a high percentage of cloud cover are convincing.

[3]The Gregg and Carder model [9] is defined for a perfectly cloud free maritime atmosphere. A fit to measurements at cloudy conditions will therefore deliver only a rough estimation of the atmospheric parameters.

8 Summary and Outlook

8.1 Summary

The context of this work is the improvement of spectral reference measurement for remote sensing applications. For remote sensing of water covered areas, the reference measurements have to be carried out in and above the water column. As over two thirds of the Earth surface is covered with water, remote sensing of deep and shallow waters is of high relevance. It is the only possibility to aquire large-scale, spatial information about large water bodies. On smaller scales, shallow water remote sensing offers a unique tool to investigate and monitor lakes and coastal areas and the influence of civilisation to them.

Measurements of under water downwelling irradiance show a very high variability, which is mainly caused by the wave-focusing effect. This effect highly influences the intensities of direct and diffuse radiation by acting similar to a lens with a highly variable geometry. The strongest influence of this effect can be observed in the upper few meters of the water column and is maximal for very small waves. To account for this well-known effect, a large number of measurements in a certain depth are necessary to calculate a reliable average. However, this number is limited due to constantly changing conditions during field measurements. As a result, measurements in depths affected by the wave-focusing effect can have large errors.

A new analytical model for the downwelling irradiance treats the direct and diffuse parts of the downwelling irradiance strictly separate. With this approach, the changes induced by the wave-focusing effect can be accounted for. The attenuation with depth roughly follows an exponential law, with the diffuse attenuation coefficient K_d as exponent. Many parameterizations exist for this parameter. But as the new model distinguishes direct and diffuse radiation, two relevant attenuation coefficients, K_dd and K_ds, are required.

In order to find a parameterization for them, numerical simulations with the well established radiative transfer model Hydro-/Ecolight 5.0 were carried out. The program was modified to simulate direct and diffuse components separately. To find a suitable parameterization for the sun zenith angle dependency of the direct irradiance component, the angular resolution of Ecolight had to be increased from 10° to 2°. The 2°-discretized phase functions were supplied by the author of Hydro-/Ecolight.

Using the numerical simulations of E_{dd} and E_{ds}, a parameterization for $\overline{K}_{\mathrm{dd}}$ and $\overline{K}_{\mathrm{ds}}$ was developed for the 10 % and 1 % light levels. An analytical description for the sun zenith dependent backscattering coefficient is included in both parameterizations. Multiple scattering is accounted for in the $\overline{K}_{\mathrm{ds}}$ model. Both attenuation coefficients are valid for absorption and scattering dominated water bodies.

In addition to the developed parameterization of K_{dd} and K_{ds}, a semi-analytical model of Pan and Zimmerman was improved concerning its sun zenith angle parameterization for the diffuse irradiance. The results of all developed parameterizations were compared to the numerical simulations. The physically meaningful, new analytical model performs better, on a wide range of simulated water compositions, than the original and even the improved Pan-Zimmerman model. On a wavelength range of 450-700 nm the new model shows an average relative deviation from the numerical results of below 2.5 % for the relevant water constituent concentration set.

To have a basis for an independent verification of the analytical model and the newly developed parameterizations for $\overline{K}_{\mathrm{dd}}$ and $\overline{K}_{\mathrm{ds}}$, field measurements at Lake Starnberg were carried out under various conditions. The downwelling irradiance was measured at varying depths and the new model was fitted to the measurements. One fit parameter, the sensor depth, was compared to independently measured sensor depths. The fits and the comparison were also performed for a model of Gordon. Due to the successful correction for the wave focusing effect, the new model yields standard deviations for the sensor depths which are smaller by a factor of five, on average, in comparison to the Gordon model results. Also the average absolute deviation has improved by a factor of about three, which is due to the newly developed parameterizations for the attenuation coefficients. The combination of both, small standard deviations and errors, finally make a reliable sensor depth determination from downwelling irradiance spectra possible.

8.2 Outlook

The comparisons of the parameterizations for depth averaged K_{dd} and K_{ds} have shown the good performance of the newly developed analytical parameterizations. However, a model which correctly accounts for the depth dependency of K_{dd} and K_{ds} can principally offer a higher accuracy than the presented model. The Pan-Zimmerman model offers this depth dependency description but couldn't account for the diffuse part's sun zenith dependency. The improvement of the Pan-Zimmerman model by the introduction of a simple sun zenith angle correction for K_{ds} shows the high potential for future developments.

The analytical parameterization of the sun zenith angle dependent backscattering coefficient

can be used to improve the model results by correctly describing the physics just below the water surface for the direct irradiance. Also at cases different from that, it turned out to be a better approximation than the common backscattering coefficient. However, analytical models for the diffuse light field above the water surface exist. If the change in light field distribution with depth could be analytically described, a physically correct backscattering coefficient, for each light field distribution and therefore depth, should be possible to develop.

The biggest advantage for the scientific community of the newly developed analytical irradiance model is the correction for the wave focusing effect. It was shown that the relative standard deviations for the estimation of the sensor depth from downwelling irradiance spectra could be significantly decreased in comparison to traditional analytical models. The new model can be exploited in various other ways, e.g. for the reliable estimation of water constituent concentrations from downwelling irradiance spectra. Also important is the fact that measurements with a high percentage of cloud cover can now be evaluated with little or no limitations, but also the average amount of measurements can be decreased, as each measurement is valid by itself and no consequent averaging is necessary. Still, further investigation of the model's performance under various illumination conditions are necessary to fully rely on these advantages.

Bibliography

[1] TriOS GmbH, TriOS Mess- und Datentechnik, http://www.trios.de.

[2] T. T. Bannister. Model of the mean cosine of underwater radiance and estimation of underwater scalar irradiance. *Limnology and oceanography*, 37(4):773–780, 1992.

[3] K. Bochter. *Das Mehrstrahl-Spektroradiometer HYDRA: Entwicklung und Einsatz zur Charakterisierung des natürlichen Lichfeldes unter und über Wasser und zur Bestimmung von Wasserqualitätsparametern.* Dissertation, DLR, 2000.

[4] R.P. Bukata. *Optical properties and remote sensing of inland and coastal waters.* CRC, 1995.

[5] P. Gege. The water color simulator WASI: an integrating software tool for analysis and simulation of optical in situ spectra. *Computers & Geosciences*, 30(5):523–532, June 2004.

[6] P. Gege and N. Pinnel. Sources of variance of downwelling irradiance in water. *Applied Optics*, 50(15):2192–2203, April 2011.

[7] H.R. Gordon. Can the Lambert-Beer law be applied to the diffuse attenuation coefficient of ocean water? *Limnology and Oceanography*, 34(8):1389–1409, 1989.

[8] H.R. Gordon, O.B. Brown, and M.M. Jacobs. Computed relationships between the inherent and apparent optical properties of a flat homogeneous ocean. *Applied Optics*, 14(2):417–427, February 1975.

[9] W.W. Gregg and K.L. Carder. A simple spectral solar irradiance model for cloudless maritime atmospheres. *Limnology and oceanography*, 35(8)(December):1657–1675, 1990.

[10] N. G. Jerlov. Marine optics. *Elsevier Oceanography Series*, 14:231, 1976.

[11] J.T.O. Kirk. Volume scattering function, average cosines, and the underwater light field. *Limnology and Oceanography*, 36(3):455–467, 1991.

[12] Z.P. Lee, M. Darecki, K.L. Carder, C.O. Davis, D. Stramski, and W.J. Rhea. Diffuse attenuation coefficient of downwelling irradiance: An evaluation of remote sensing methods. *Journal of Geophysical Research-Oceans*, 110(C2), 2005.

[13] C.D. Mobley. *Light and water: Radiative transfer in natural waters*. Academic Press, 1994.

[14] C.D. Mobley, L.K. Sundman, and Emmanuel Boss. Phase function effects on oceanic light fields. *Applied Optics*, 41(6):1035–1050, February 2002.

[15] C.D. Mobley and Lydia K. Sundman. Hydrolight 5.0 Users Guide. Technical report, DTIC Document, 2008.

[16] M. Nicolaus, S.R. Hudson, S. Gerland, and K. Munderloh. A modern concept for autonomous and continuous measurements of spectral albedo and transmittance of sea ice. *Cold Regions Science and Technology*, 62(1):14–28, June 2010.

[17] X. Pan and R.C. Zimmerman. Modeling the vertical distributions of downwelling plane irradiance and diffuse attenuation coefficient in optically deep waters. *Journal of Geophysical Research*, 115(C8):C08016, 2010.

[18] T.J. Petzold. Volume scattering functions for selected ocean waters. Technical Report 3, DTIC Document, 1972.

[19] J.R.V. Zaneveld, E Boss, and A Barnard. Influence of surface waves on measured and modeled irradiance profiles. *Applied Optics*, 40(9):1442–1449, March 2001.

Danksagungen

An erster Stelle möchte ich mich bei meinem Betreuer, Peter Gege, bedanken. Er hat es immer wieder geschafft sich in meine Probleme hineinzuversetzen und sein Wissen auf Augenhöhe weiterzuvermitteln. Eine bessere Betreuung hätte ich mir nicht wünschen können!

Ohne die tatkräftige und uneigennützige Hilfe von Patrick Wolf und Sebastian Rößler von der Limnologischen Station Iffeldorf, wären meine Feldmessungen undenkbar gewesen und hätten auch nicht annähernd so viel Spaß gemacht! Aber auch der restlichen Belegschaft der Station sei gedankt für die vielen netten Stunden in Iffeldorf!

Meiner Abteilung am DLR in Oberpfaffenhofen möchte ich danken für die schöne und angenehme Zeit am Institut, den Kaffeerunden, Kletterabenden und Grillfesten!

Dem Autor von Hydrolight, Curtis Mobley, möchte ich besonders danken für seine tatkräftige Hilfe bei den diversen Anpassungen an seinem Programm, die die Grundlage für meine guten Ergebnisse darstellen.

Vielen Dank natürlich an die vielen Korrekturleser meiner Arbeit, allen voran an meinen Patenonkel, Thomas Andrich. Danke auch an Martin Mannes und Karim Lenhard!

Ein nicht unerheblicherer Anteil an Dank gebührt meinen moralischen Unterstützern, Franz Muschter und Andrea Böttcher!

Und nicht nur weil es eben selbstverständlich ist seine Eltern zu erwähnen, gebührt den beiden, Sabine Grötsch und Thomas Schneider, mehr als nur ein bloßer Dank: ohne euch hätte ich es nicht so weit gebracht! Ihr habt mich immer unterstützt, in dem was ich gemacht habe und habt mir - fast noch wichtiger - dabei das Gefühl gegeben, dass es auch das Richtige ist!

Last but not least, möchte ich der Entwicklercommunity von Python danken - ohne diese geniale Programmiersprache hätte ich unter keinen Umständen meine Auswertung in diesem Umfang realisieren können!

Ich versichere, diese Arbeit selbstständig angefertigt und dazu nur die im Literaturverzeichnis angegebenen Quellen benutzt zu haben.

München, den 25. Juli 2011